





Geophysical Trends Inferred From 20 Years of AIRS Infrared Global Observations

S. DeSouza-Machado¹ , L. Larrabee Strow^{1,2} , and R. J. Kramer³ 

¹JCET/GESTAR2, University of Maryland Baltimore County, Baltimore, MD, USA, ²Department of Physics, University of Maryland Baltimore County, Baltimore, MD, USA, ³NOAA GFDL, Princeton, NJ, USA

Key Points:

- The 20+ year radiance record of NASA's Atmospheric Infrared Sounder contains detailed vertical information about changes in geophysical parameters
- We introduce an algorithm to retrieve climate geophysical trends from radiance observations, using stable channels and traceable *a priori*
- Comparisons are made to trends from monthly reanalysis geophysical fields and L3 operational retrieval data products

Correspondence to:

S. DeSouza-Machado,
sergio@umbc.edu

Citation:

DeSouza-Machado, S., Strow, L. L., & Kramer, R. J. (2025). Geophysical trends inferred from 20 years of AIRS infrared global observations. *Journal of Geophysical Research: Atmospheres*, 130, e2025JD043501. <https://doi.org/10.1029/2025JD043501>

Received 27 JAN 2025

Accepted 17 JUL 2025

Author Contributions:

Conceptualization: L. Larrabee Strow
Formal analysis: S. DeSouza-Machado
Funding acquisition: L. Larrabee Strow
Investigation: S. DeSouza-Machado
Methodology: S. DeSouza-Machado, L. Larrabee Strow, R. J. Kramer
Resources: R. J. Kramer
Software: S. DeSouza-Machado
Supervision: L. Larrabee Strow
Validation: S. DeSouza-Machado, L. Larrabee Strow, R. J. Kramer
Writing – original draft: S. DeSouza-Machado
Writing – review & editing: S. DeSouza-Machado, L. Larrabee Strow, R. J. Kramer

© 2025. The Author(s). This article has been contributed to by U.S. Government employees and their work is in the public domain in the USA.
 This is an open access article under the terms of the [Creative Commons Attribution-NonCommercial](https://creativecommons.org/licenses/by-nc/4.0/) License, which permits use, distribution and reproduction in any medium, provided the original work is properly cited and is not used for commercial purposes.

Abstract Daily spectral radiance observations by NASA's Atmospheric Infrared Sounder contain detailed information about surface and atmospheric temperature and water vapor. We obtain climate geophysical trends from 20 years (2002/09–2022/08) of Atmospheric Infrared Sounder (AIRS) observations using a novel method operating mostly in radiance space. The observations are binned into 3×5 degree tiles using 16 day intervals, after which nominally clear scenes are selected for each tile to construct the spectral radiance time series. Deseasonalized spectral trends are then obtained, which are inverted using a physical retrieval to obtain geophysical trends. This approach is distinct from traditional use of radiances whereby trends are generated after operational retrievals or assimilation into Reanalysis models. Our approach rigorously ties the derived geophysical trends to the observed radiance trends, using far fewer computational resources and time. The retrieved trends are compared to trends derived from ERA5 and MERRA2 reanalysis geophysical fields, and NASA Level3 AIRS v7 and CLIMCAPS v2 data. Our retrieved surface temperature trends agree quite well with ERA5, CLIMCAPS, and the GISS surface climatology trends. Atmospheric temperature profile trends exhibit some variability among all these data sets, especially in the polar stratosphere. Water vapor profile trends are nominally similar among the data sets except for the AIRS v7 which exhibits drying trends in the mid troposphere. Spectral closure between observed trends and those computed by running the reanalysis and AIRS L3 monthly retrieval products through a radiative transfer code are discussed, with the major differences arising in the water vapor sounding region.

Plain Language Summary The current generation of infrared sounders, designed for weather forecasting purposes, have been operational for a long enough time to enable anomaly and trending studies for climate purposes. The daily radiance observations are routinely used for operational atmospheric state retrievals and assimilation into reanalysis models, after which climate anomaly studies are enabled. Here we use a purpose built algorithm to directly turn radiance observations into geophysical anomalies and trends with full error characterization. This unique approach for observational climate trending uses only stable low noise sounding channels, easily understood assumptions and well-tested retrieval algorithms, purpose-built for generating climate data products.

1. Introduction

Accurate, stable observational records of global temperature and water vapor are foundational to our ability to monitor, understand, and predict climate variability and change. As atmospheric concentrations of non-condensing Greenhouse Gases (GHG) such as CO₂ rise (Friedlingstein et al., 2022; Keeling et al., 1976), the gradually increasing opacity of the atmosphere prompts responses in temperature and water vapor throughout the atmospheric column that feed back on Earth's radiative energy budget. Like a controlling knob on the climate, the precise magnitude of these changes is a key determinant of the amount of GHG-induced planetary temperature, precipitation and circulation change that Earth has experienced so far, and may experience in the future (Held & Soden, 2000; Manabe & Wetherald, 1967; Muller et al., 2016; Schneider et al., 2010). Consequently, observations of multi-decade temperature and water vapor trends have proven critical for confirming GHG-induced climatic changes are occurring in nature and for monitoring and attributing its evolution over time. Vertically-resolved information content in these measurements has been particularly important for confirming the influence of human activities on the climate. Spatially-resolved, observed trends have been used to identify the fingerprints of CO₂ effects on the profile of temperature change (B. D. Santer et al., 1996; Thorne et al., 2011) and on upper-tropospheric water vapor changes (Allan et al., 2022; Chung et al., 2014; Soden et al., 2005). Long-term records of temperature and water vapor profiles are also routinely used to monitor the drivers of unprecedented

increases in Earth's energy imbalance observed in recent years (Kramer et al., 2021; Loeb et al., 2021). Key documents which further underscore the importance of accurate measurements of global temperature and humidity include the Intergovernmental Panel on Climate Change (IPCC) reports (see e.g., Houghton et al., 1990; IPCC, 2021).

Data of past temperature and water vapor variability, with the global coverage necessary for climate analysis, often comes from two main sources: satellite observations or reanalysis. While these sources have been groundbreaking for our ability to monitor and understand the climate, in their current form, both can often be deficient for the quantification of anomalies and trends. Reanalysis approaches (Gelaro et al., 2017; Hersbach et al., 2020; Kalnay et al., 1996), which require an assimilation system and dynamic model, have not traditionally been developed for the purpose of climate trend evaluation, and may give inaccurate trends because of one or more of the following reasons (Cai & Kalnay, 2004; Kistler et al., 2001; Shao et al., 2023): they typically use observing systems that change with time as new in situ or satellite based instruments become operational, the observations may have biases and errors that are not correctly accounted for, the assimilated observations may be obtained (or simply not available) in cloud conditions, the dynamical models cannot contain all the physics (e.g., land topography, cloud microphysics) at the finite sized grid boxes used, and often do not use for example, time varying concentrations of CO₂ or stratospheric aerosols. While modern reanalysis systems have better addressed these issues (Dee et al., 2011), many of these issues remain, particularly in data sparse regions (Bromwich et al., 2024; Hobbs et al., 2020).

Satellite based observations covering the Earth started in the 1970s and currently operational instruments cover almost the entire electromagnetic spectrum, providing valuable information about the Earth's surface and atmosphere. These include passive microwave and infrared sounders that provide global information about temperature and humidity 24 hr a day. In this paper we focus on 20 years of observational data (September 2002–August 2022) from NASA's Atmospheric Infrared Sounder (AIRS), which is an infrared nadir sounder. Even when a satellite instrument provides long, radiometrically stable measurements, such as AIRS as described in the next Section, the downstream data products used by the scientific community still can suffer from deficiencies in their usefulness for climate trend and anomaly analysis. Through the retrieval process, the conversion of a stable, level 1 radiance record into a level 2/3 geophysical product can often introduce data sampling biases, loss of error traceability, and instabilities from an a priori that render the final product less appropriate for trend analysis than the initial radiance record. These issues can be exacerbated when a geophysical record must stretch across successive instruments with different sensor characteristics, cal/val approaches and algorithm development, especially when the data value chain is not designed with climate continuity prioritized (KISS Continuity Study Team, 2024). Given strong sensitivity of IR Sounders to clouds, AIRS retrievals of temperature and moisture are particularly challenging and susceptible to the introduction of the retrieval uncertainties described above. Operational NASA AIRS daily Level 2 products and monthly Level 3 products (derived from Level 2) used in this paper retrieve the atmospheric state using cloud-cleared radiances derived from a 3 × 3 grid of individual scenes. A main characteristic of traditional L2 retrievals is the requirement for a good a priori state for each inversion, making errors in the a priori difficult to distinguish from true variability in the observations.

Measurements by visible imagers which have ~1 km horizontal resolution or better (King et al., 2013) suggest global cloud free fractions of ~30%, but the 15 km footprint of typical sounders means at most 5% of the hyperspectral observations can be considered “cloud-free.” Current operational NASA L2 products for AIRS use the method of cloud clearing on observed radiances in partly cloudy scene conditions before doing the geophysical retrieval. The cloud clearing method takes in the raw observed all-sky radiances and solves for an estimate of clear column radiances by examining adjacent Fields of View (FOVs) to estimate the cloud effects on the observations. The method assumes any differences are solely due to different cloud amounts in each FOV, and significantly increases geophysical retrieval yields (to about 50%–60%) (Smith & Barnet, 2023). The resulting cloud cleared radiances (CCR), distinct from clear sky radiances which are obtained under nominally clear conditions, have increased noise especially in the lower atmosphere sounding channels; in addition the subsequent retrieval depends on the first guess (which is a neural net for AIRS v7 and MERRA2 reanalysis for CLIMCAPS v2). The reader is referred to AIRS L2 literature (Smith & Barnet, 2020, 2023; Susskind, 2006; Susskind et al., 2003, 2014) for more details about cloud clearing and the L2 algorithms.

Geophysical retrievals are necessary for many climate applications and Level 2/3 products are heavily used by the climate research, modeling and monitoring community. Some loss of climate applicability of the data due to the retrieval process is inevitable. However, shortcomings of the community's reliance on retrieval products not specifically designed for climate analysis have become increasingly apparent. For instance, He et al. (2021) estimated temperature and water vapor feedbacks from multiple reanalysis and Level 3 products in an attempt to constrain climate models, but found the spread across the observation-based estimates was larger than that of the models. This paper introduces novel AIRS temperature and water vapor satellite retrievals specifically tailored for climate analysis, and evaluates them relative to a suite of legacy Level 2/3 satellite and reanalysis data products.

1.1. Using Hyperspectral Infrared Radiance Observations Directly for Climate Trending

We have designed an algorithm that remains in hyperspectral infrared radiance time-series space to the maximum extent possible, preserving the full thermodynamic and trace gas information contained in the well-characterized and well-understood AIRS radiances (Strow & DeSouza-Machado, 2020), before performing a thermodynamic trend retrieval using the well-known Optimal Estimation (OEM) Rodgers (2000) retrieval algorithm. Moreover, our novel approach has zero temperature *a priori* and minimal water vapor *a priori*. This completely sidesteps time variability and the accuracy of the *a priori* which causes errors in the retrievals, and ensures our work examines trends directly inferred from the radiances versus those from traditional methods. This yields more unbiased results which highlight where the sensor has limited sensitivity, for example, in retrieving boundary layer or stratospheric water vapor.

Our approach is a significant refinement on the traditional “retrieve/assimilate then process” method which starts with observational radiance observations, then produces geophysical variables using L2 retrieval algorithms or assimilation into dynamical engines of reanalysis models, and finally computes climate anomalies or trends. The key components of the retrieval and reanalysis models are not tailored for climate anomalies or trending. In addition reanalysis and Level 2/3 products require large computational resources that preclude rapid full data set re-processing to help fully understand trends; the work presented here, once the averaged/sorted observations are available, can be processed in hours to days, and can easily be duplicated by small research groups as well as adapted to study climate anomalies.

Applying our algorithm to AIRS observations is particularly advantageous, not just because of its long record length, but because the hyperspectral measurements it provides are particularly useful for climate analysis, which typically requires a granular decomposition of broadband radiative changes. Passive microwave and infrared instruments with handfuls of channels have also been flown since the late 1970s for meteorological purposes. For example, the Microwave Sounding Unit (MSU) and Advanced Microwave Sounding Unit (AMSU) provide global scale records of upper atmospheric temperatures (Mears & Wentz, 2009, 2016). Another example is the 20 channel High resolution Infrared Radiation Sounder (HIRS) (Harries et al., 1998; Menzel et al., 2016; Shi & Bates, 2011), which provides an ~ 40+ year global observational data set. However, these instruments have limitations which constrain climate studies including: broad vertical weighting functions which only allows for limited vertical resolution, drifts of the orbits or instruments, as well as the need to inter-calibrate the individual instruments (lifetimes ~5–10 years). For example, the water vapor feedback is very sensitive to the H₂O changes in the thinner layers extending between the cold dry upper troposphere and lower stratosphere, while the HIRS instrument upper tropospheric water vapor sensitivity is a 200–500 mb thick layer (Muller et al., 2016).

These limitations have largely been mitigated by the new generation of infrared sounders, which have high spectral resolution (which gives superior vertical resolution), are radiometrically very stable (~0.002 K/year or better) and whose overlapping orbits and long lifetimes allows for continual inter-calibration and monitoring of the stability of these instruments; see for example, (Strow et al., 2021). AIRS is the first of the new generation of low noise, high stability hyperspectral sounders, and has been in almost continuous operation since September 2002, making Top of Atmosphere (TOA) radiance observations at a typical 15 km (at nadir) horizontal resolution. Instruments with similar characteristics and abilities include the ESA's Infrared Atmospheric Sounding Interferometer (IASI) and NOAA's Cross-track Infrared Sounder (CrIS), operational since June 2007 and March 2012, respectively. The latter two already have followed on missions planned till the 2040s, and together these three sounders will provide scientists with a 40 year high quality, near continuous observational data set for climate studies.

Infrared radiances contain a wealth of information. A short list focusing on scientific contributions using the AIRS radiance observations includes improvements in surface temperature, atmospheric temperature and water vapor profiles in weather forecasting models (see e.g., LeMarshall et al., 2006; Andersson et al., 2007), retrieving mixing ratios of greenhouse gases such as CO₂ (Chedin et al., 2005), CH₄ (Zou et al., 2019), and O₃ (Fu et al., 2018). Clouds (Kahn et al., 2005, 2014) and large aerosols (volcanic ash and dust) (Carn et al., 2005; De Souza-Machado et al., 2010) can also be detected and quantified. Examples of other trace gases that can be detected and quantified are CO (McMillan et al., 2005) and NH₃ (Warner et al., 2016). This list is not exhaustive and in addition multiple papers have similarly been published using CrIS and IASI data.

The stability and accuracy of the AIRS instrument is documented in recent work on analyzing 16 years of AIRS radiance anomalies over cloud-free ocean (Strow & DeSouza-Machado, 2020). Geophysical retrievals on the anomalies yielded CO₂, CH₄, N₂O, and surface temperature time series that compared well against in situ NOAA Global Monitoring Laboratories (GML) trace gas measurements and NOAA Goddard Institute of Space Studies (GISS) surface temperature data, respectively. A significant difference between this paper and (Strow & DeSouza-Machado, 2020) is the nominally clear scenes used in this paper are selected uniformly using tiles covering the whole Earth, while the clear scenes in the latter were zonal averages which were sometimes concentrated in certain regions. The tiles containing the AIRS measurements are of size $\sim 3^\circ \times 5^\circ$, chosen such that the number of observations in each tile is roughly equal. Nominally clear scenes for each tile are picked out using a quantile approach; from the time series, radiance trends are made over the entire Earth, from which geophysical trends are retrieved.

Observed infrared spectral trends from AIRS has already been a focus of earlier work by (X. Huang et al., 2023) who studied a slightly shorter time period (2002–2020) using the nadir L1B radiance observations (which have no or minimal frequency corrections compared to the L1C radiance data set we use here). Similarly the paper by Raghuraman et al. (2023) converted the AIRS observed radiances to Outgoing Longwave Radiation (OLR) in the 0–2000 cm^{−1} range, but neither of these studies involve retrieving geophysical trends from radiance spectral trends. Instead, they include the effects of GHG forcings and convert various reanalysis geophysical trends (such as ERA5) to spectral trends for comparison against the observed spectral trends, which we also show in Appendix B. Teixeira et al. (2024) used the AIRS observations between 2003 and 2012 to measure the impact of increased CO₂ on the outgoing radiances. Another noteworthy examination of the time evolution of high spectral resolution infrared radiances (converted to spectral outgoing longwave radiation (OLR) fluxes) by Whitburn et al. (2021) covered 10 years (2007–2017) of IASI observations. They confirmed that the IASI-derived fluxes agreed well with increases in GHG gas concentrations and El-Nino Southern Oscillation (ENSO) events within that time frame. A more recent paper (Roemer et al., 2023) used the 10 year IASI observations to derive all-sky longwave feedback spectral components (water vapor, CO₂, window, and ozone) and total values, while also estimating clear sky feedback values. Other relevant studies involving high spectral resolution infrared measurements include the all-sky inter-annual variability at different spatial scales using 5 years (2007–2012) of IASI observations (Brindley et al., 2015), and comparing Global Climate Model simulations to AIRS radiances as a diagnostic of model biases (Y. Huang et al., 2007).

We will refer to our results as the AIRS Radiance Trends (AIRS_RT). Comparisons are made against monthly output from the European Center for Medium Weather Forecast fifth generation reanalysis (ERA5) (Hersbach et al., 2020) and NASA's second generation Modern-Era Retrospective analysis for Research and Applications (MERRA2) (Gelaro et al., 2017), and also against the official monthly AIRS L3 products which are AIRS v7 L3 (Susskind et al., 2014; Tian et al., 2020) and CLIMCAPS v2 L3 (Smith & Barnett, 2019, 2020). Detailed noise estimates for the underlying radiance time series are given in Appendix A. Geophysical trends and spectral closure studies are presented for the averaged ascending (daytime (D)) and descending (nighttime (N)) trends; Appendix B briefly discusses separate D and N trends.

2. Data Sets Used in This Study

Three main types of data sets are used in this study. The first is the AIRS L1C radiance observation data set we analyze for this paper, which has both daytime (D) and nighttime (N) (ascending and descending) views of the planet. Second is the monthly operational L3 retrieval data, which are the AIRS v7 and the CLIMCAPS v2 products, also separated into D/N subsets. Finally, we also compared trends from ERA5 and MERRA2 monthly reanalysis of geophysical fields. The ERA5 monthly data set is available in 8 averaged time steps, so we match to

the average AIRS overpass times and separate into (D/N) sets over the 20 years, while MERRA2 monthly geophysical output fields are only available as one time step; included here for completeness we mention the NASA GISS surface temperature data set, which like MERRA2 is only available as a monthly mean. This means four of the data sets: AIRS_RT (from AIRS L1C), AIRS L3 and CLIMCAPS L3 operational retrievals, and ERA5 are separable into D/N, while the other two (MERRA2 and GISS) are only available as a diurnal averaged value. We describe these data sets in more detail below.

2.1. The AIRS Instrument and L1C Observational Data Set

The Atmospheric Infrared Sounder (AIRS) on board NASA's polar orbiting EOS/Aqua platform has 2,378 channels, covering the Thermal Infrared (TIR) spectral range (roughly 649–1613 cm^{-1}) and shortwave infrared (2181–2665 cm^{-1}). The Aqua platform is a polar orbiting satellite with 1.30 a.m. descending (night time over equator) and 1.30 p.m. ascending (daytime over equator) tracks. Each orbit takes about 90 min, with the 16 passes yielding almost twice daily coverage of the entire planet, with about ~ 3 million AIRS spectral observations obtained daily. AIRS became operational in late August 2002 and has provided observations almost continuously since, with occasional shutdowns (each spanning a few days) such as during solar flare events.

AIRS channel full widths at half maximum satisfy $\nu/\delta\nu \sim 1200$ with (spectral dependent) noise typically ≤ 0.2 K, though it rises to ~ 1 K at the 15 μm (645 cm^{-1}) end. The original L1b radiance observations suffer from spectral gaps and noise contamination as detectors slowly fail. These limitations are addressed using a 2645 L1c channel observational data set (AIRS Project Office, 2015), where spectral gaps and some of the noise “pops” are filled in using principal component reconstruction (Manning et al., 2020). The channel frequency shifts that appear in the L1b product have been essentially completely removed in L1c (AIRS Project Office, 2015) and is the data set used in this paper. The frequency calibration received a further adjustment after 23 September 2021 for a frequency shift caused by a deep space maneuver performed for checking the radiometric polarization corrections. The results described in this paper use only the actual observed radiances in pristine channels stable to 0.002 K/year as described in Strow et al. (2021), which have been shown to produce accurate CO_2 , SST, CH_4 trends. The shortwave (SW) channels are drifting at a higher rate than the LW/MW channels, which can lead to incorrect surface temperature rates, and are avoided in this paper. Similarly there are many channels in the LW and MW whose A-only and B-only detectors are drifting in time, and which are also not used here. For example, we avoid using some higher wavenumber (shorter wavelength) channels past the ozone band which have a significant drift in time, possibly due to changes in the polarization of the scan mirror coating with time. Therefore, compared to other AIRS operational products used in this paper, our results use channels that are demonstrated to have high stability (Strow et al., 2021). We do note that some of the observed drifts in the AIRS channels stabilized after 6 years, so their impact is reduced when looking at 20 year trends.

Observational data spanning 20 years (1 September 2002–31 August 2022) of AIRS L1C radiance observations are gridded into 4,608 tiles covering the Earth: 72 longitude boxes which are all 5° in width, and 64 latitude boxes which are approximately 2.5° in width at the tropics but wider at the poles to keep the number of observations per 16 day intervals (which is the repeat cycle of the AIRS orbit on the Aqua satellite) roughly the same. This way there are $\sim 12,000$ observations per 16 days per tile, which are roughly equally divided between the ascending/daytime (D) and descending/nighttime (N) tracks. In this paper we discuss results for both the ascending and descending tracks using a retrieval based on the longwave (LW) and midwave (MW) regions of the spectrum (640–1620 cm^{-1} or 6–15 μm).

2.2. Reanalysis Geophysical Fields

The ERA5 fifth generation reanalysis product from the European Center for Medium Range Weather Forecasts is freely available on monthly timescales from the Copernicus Climate Data Store. This monthly data set is output at 37 pressure levels at 0.25° horizontal resolution (Hersbach et al., 2020), which is further subdivided into eight 3-hr averages per month (corresponding to 00, 03, 06, ... 21 UTC). For each month from September 2002 to August 2022 we downloaded the surface temperature and pressure fields, as well as atmospheric temperature, water vapor and ozone fields. These are then colocated to each tile center using 2D spatial interpolation, as well as time interpolated according to the average AIRS overpass time as a function of month. From the resulting monthly time series of reanalysis geophysical fields for each tile, we generated (a) thermodynamic trends for surface temperature, air temperature, water vapor and ozone fields (b) a 20 year average thermodynamic profile in order to

produce Jacobians for the linear trend retrievals (c) by using the geophysical fields as input to the clear sky SARTA radiative transfer code (Strow, Hannon, DeSouza-Machado et al., 2003) a monthly time series of clear sky radiances for each tile was generated, from which we could compute radiance trends. The matching to ERA5 reanalysis was done for both the ascending and descending observations.

The MERRA version 2 (MERRA2) reanalysis used in this paper is the second generation (Gelaro et al., 2017) product from NASA's Global Modeling and Assimilation Office. The monthly data we use is available on 42 pressure levels at a horizontal resolution of $0.5^\circ \times 0.625^\circ$, but only one monthly mean diurnally averaged output is available per month. Similar to the ERA5 output, we colocated the MERRA2 surface temperature, atmospheric temperature, water vapor and ozone fields to our tile centers for each month starting September 2002 in order to produce a time series of geophysical and computed radiance output, from which radiance and thermodynamic trends could be computed for comparisons against other data sets in this study; similar to above we also generated a monthly time series of clear sky radiances for each tile, from which we could compute clear sky radiance trends based on MERRA2.

The NASA Goddard Institute of Space Studies (GISS) v4 surface temperature data (GISTEMP Team, 2025; Lenssen et al., 2019, 2024) is a 1,200 km smoothed monthly data set based primarily on near surface temperatures land stations, and data from ships and buoys. As with MERRA2 we obtained one monthly mean data set per month, which we could not separate into descending (N) or ascending (D) tracks.

2.3. AIRS L3 Operational Retrieval Products

NASA routinely produces two retrievals from the daily AIRS L1C observations, which are AIRS v7 (Susskind et al., 2014; Tian et al., 2020) and CLIMCAPS v2 (Smith & Barnett, 2019, 2020). Both use the cloud clearing process but there are significant algorithmic differences; in particular the AIRS v7 product is initialized by a neural net, while CLIMCAPS uses MERRA2 for its initialization. The L2 retrieval products are then individually turned into L3 monthly retrieval products, for both the ascending (daytime) and descending (nighttime) observational data. The time series of thermodynamic profiles were used as input to the clear sky SARTA RTA to generate radiances, after which radiance trends and thermodynamic trends are also produced.

2.4. Other L3 Operational Retrieval Products

The Microwave Limb Sounder (MLS) monthly binned water vapor (H_2O) mixing ratio data set (Lambert et al., 2007, 2021; Livesey et al., 2006), which contains retrieved fields covering $\pm 82^\circ$ latitude, at a spatial resolution of $4^\circ \times 5^\circ$ and useful vertical range between 316 and 0.00215 hPa was used in this paper to improve retrieval trends in the upper atmosphere.

3. Filtering the Observational Radiance Data for Clear Scenes

In the following sections, we explain the novel AIRS_RT algorithm and provide testing and justification of the specific choices made. In this section we discuss the “clear scene” selection from all the observed data stored for each of the 72×64 tiles. Ideally, we would prefer to use a MODIS cloud fraction product (1 km) colocated to the 15 km AIRS footprints, but this is presently unavailable. Our earlier work used an uniform clear flag over ocean (Strow et al., 2021) which will not work well over land because of surface inhomogeneity. In this section, we discuss an alternative clear filter based on the hottest 10% of AIRS observations that are present inside any 16 day tile, over any location.

3.1. Observed BT1231 Distributions

The radiances measured in thermal infrared window region ($800\text{--}1000\text{ cm}^{-1}$ and $1100\text{--}1250\text{ cm}^{-1}$) are dominated by the effects of the surface temperature, water vapor continuum absorption and cloud/aerosol effects. The effects of water vapor continuum absorption is largest in hot and humid tropical scenes (depressing the observations relative to surface temperatures by about 5–6 K, which reduces to about 2 K at $\pm 50^\circ$) and is almost negligible for cold, dry scenes (less than 1 K). Scattering and absorption by liquid and ice clouds also affects the window region (Deep Convective Clouds can depress the window channel observations by as much as 100 K relative to surface temperatures). For each tile, we use the 1231.3 cm^{-1} observation as our representative window channel (AIRS L1C channel ID = 1520), as it is minimally impacted by weak water vapor lines. Changed to

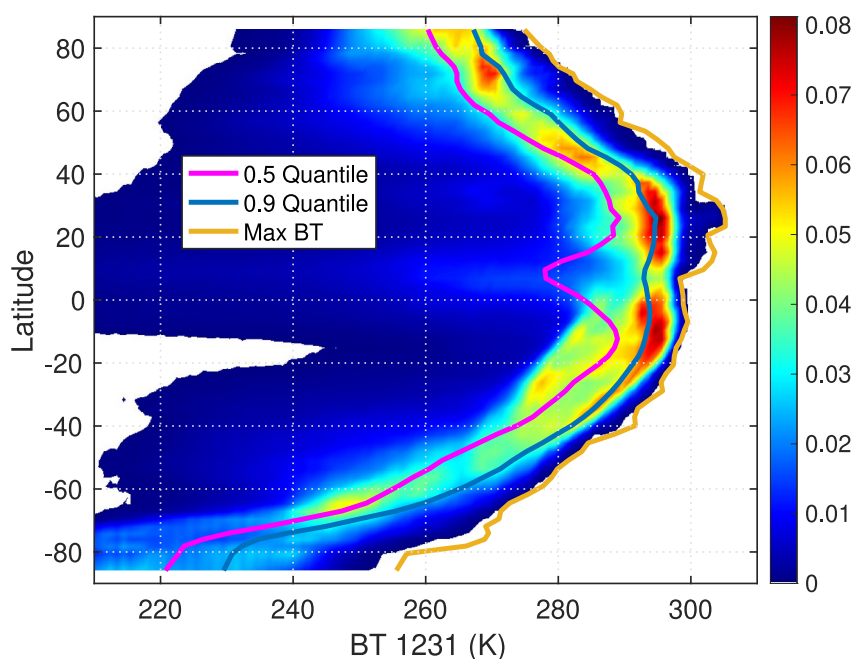


Figure 1. Zonally averaged BT1231 normalized histograms (probability distribution functions (pdf)) as a function of latitude and temperature bin, for the 16 day timespan between 2012/08/27–2012/09/11. The vertical axis is in degrees Latitude and the horizontal axis units are in Kelvin, while the color bar units for the pdfs are in normalized counts per Kelvin. We also plot quantile curves $Q0.XY$ which stand for the actual numerical value of the BT1231 quantile, as explained in the text. The blue curve is the $Q0.90$ quantile used in this paper, and is very close to the maximum $Q1.00$ quantile. For clarity we have not shown other “warmer” quantiles such as $Q0.80$, $Q0.95$ since they are offset very close to the left and right of $Q0.90$, respectively. The 210 K cutoff means we do not show the tail of the distribution of the observations over the winter polar regions, or the extremely cold DCC in the tropics.

Brightness temperature (BT) the observation in this 1231.3 cm^{-1} channel (BT1231) therefore serves as a measure for the cloudiness of an observation: if there are no or low or optically thin clouds, it will effectively measure the surface temperature, but as the clouds get thicker and higher, it will measure the cold cloud top temperatures. For every tile during any 16 day observation periods, we compute quantiles Q based on the observed BT1231 to design a filter that chooses between cloudy and partially clear scenes. We describe below the testing of the different BT1231 quantiles (where quantile $Q0.XY$ will have a numerical value $BT1231_{Q0.XY}$ associated with it) to determine which value best provides nominally clear scenes for every tile (over ocean and land) that agree with other nominally clear data sets we have used previously (Strow & DeSouza-Machado, 2020). Figure 1 shows all the BT1231 observations for a chosen 16 day timestep in the form of a zonally averaged histogram (normalized probability distribution functions (PDFs)), with latitude on the vertical axis and BT1231 on the horizontal axis. The color bar is the PDF value, and we used observations spanning 27 August 2012–11 September 2012 which is approximately half way through the 20 year AIRS mission data set used in this paper. The curves show the zonally averaged BT1231 values of the median ($Q0.50$ in magenta), maximum ($Q1.00$ in gold) and $Q0.90$ in blue curves. We did not show other warmer quantiles such as $Q0.80$, $Q0.95$ and $Q0.97$ since they are only slightly offset, either to the left (cooler) or right (warmer) as appropriate, relative to the $Q0.90$ curve. The exception is that at the equator, $Q0.80$ still has the remnants of lower temperatures due to clouds and is slightly cooler, as similarly seen in the behavior of the mean and median curves. The distributions are skewed to the left (negative skewness), as confirmed by the mean being less than the median. The very cold (190 K) observations over the winter Antarctic are not seen as we use a 220 K horizontal axis cutoff. The figure shows the expected qualitative features, for example, (a) the tropical PDFs peak at around 295 K, but show some warmer observations, as well much colder observations (below 230 K) corresponding to Deep Convective Clouds (DCC); this gives a dynamic range of almost 100 K at the tropics (b) the BT1231 observed over the Southern Polar (polar winter) regions are much colder than the BT1231 observed over the Northern Polar (polar summer) regions, and (c) the reddish peaks in the 30°N – 40°N are a combination of the marine boundary layer (MBL) clouds and warmer summer land temperatures. Figure 1 shows on average the cloud effect at the tropics is an additional modest 20 K (difference between

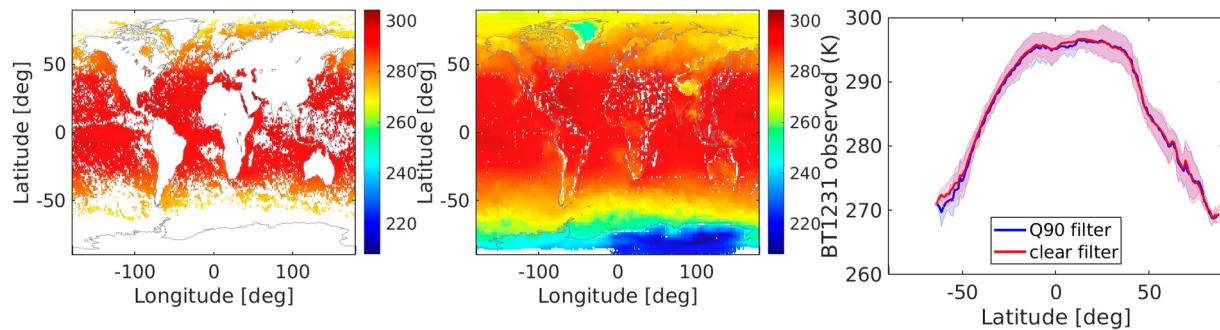


Figure 2. Clear scenes for the same 2012/08/27–2012/09/11 timespan selected by (left) a uniform/clear sky filter and (center) the Q0.90 BT1231 average described in this paper. The color bars for the left and center plots are in Kelvin. The right hand plot shows the mean (over ocean) observed BT1231 (vertical axis, in Kelvin) as a function of latitude, for the two selections; the difference is about $0 \text{ K} \pm 1 \text{ K}$ in most regions except in the southern midlatitudes where the Q0.90 average produced scenes that were about 1 K cooler on average. Note that in this and subsequent figures, Q0.90 is the average of all data points values between Q0.90 (shown in Figure 1) and the maximum, using observed BT1231 as the discriminator as explained in the text.

Q0.90 and Q0.50) compared to the 100 K dynamic range. This is because the cloud fractions and cloud decks in the individual observations have effectively more clouds (with larger cloud fraction in the FOV) lower in the atmosphere than higher up; the net effect is that in the window region the atmosphere is on average radiating from the lower (warmer) altitudes, and so spectra whose BT1231 values are larger than $BT1231_{Q0.80}$, see much of the surface emission as well.

We now use the above plots to select “almost clear” scenes. For any one tile, we define set $\Psi_{0.XY}$ to have all observations i whose BT1231 lies between quantiles Q0.XY and Q1.00, $\{i | BT1231_{Q0.XY} \leq BT1231(i) \leq BT1231_{Q1.00}\}$. In what follows Q0.XY is the radiances averaged over all the observations i which are in the set $\Psi_{0.XY}$, namely

$$r_{Q0.XY}(\nu) = \frac{1}{N_{0.XY}} \sum_{i \in \Psi_{0.XY}} r_i(\nu) \quad (1)$$

where $r_i(\nu)$ are the $N_{0.XY}$ individual observations in set $\Psi_{0.XY}$. In this section, we only use the $\nu = 1231 \text{ cm}^{-1}$ channel, but in later sections we easily form averages for all 2,645 channels, at any 16 day time step for any tile.

We tested different quantile sets $\Psi_{0.XY}$ to see which one can reliably be considered to provide a nominally “cloud free” global observational data set, and chose the Q0.90 average (i.e. defined as averaged over the $\Psi_{0.90}$ set, which spans Q0.90 to Q1.00) as the one to use for the rest of this paper, unless explicitly stated otherwise. The tests primarily involved comparisons to scenes produced by the uniform/clear sky filter described in (Strow & DeSouza-Machado, 2020) for the same 27 August 2012–11 September 2012 16 day timespan. This latter filter selects clear scenes by both testing for uniformity (to within 0.5 K) across a 3×3 grouping of AIRS scenes and also using a criteria that the observed window channel observations should be within $\pm 4 \text{ K}$ of clear-sky simulations using thermodynamic parameters supplied by reanalysis models. The results are shown in the left hand plot of Figure 2, plotted on a $1^\circ \times 1^\circ$ grid. We note in this plot the uniform/clear scenes that are plotted are limited to those over ocean, and for solar zenith less than 90° (daytime), which automatically filtered out many of the views over the (wintertime) Southern Polar region. Immediately apparent are the gaps produced by the uniform/clear filter, for example, in the Tropical West Pacific or off the western coasts of continents where there are clouds. The gaps can be changed by, for example, changing the 4 K threshold to allow more or fewer scenes through the filter.

The center plot shows for all tiles, the daytime scenes selected by the Q0.90 filter for the same time period, on the same $1^\circ \times 1^\circ$ grid. Compared to the left hand plot, the spatial coverage is almost complete, as the Q0.90 average always has the hottest 10% of the observations. At this 1° resolution, used for comparison with the uniform/clear grid filter described in the previous paragraph, gaps are seen in regions where for example, the local topography means observations over mountains would be colder than the surrounding coastal or plain regions. This is not a

concern since zooming back out to the coarser $3^\circ \times 5^\circ$ tile resolution, will include Q0.90 observations for the quantile and trending analysis.

To compare the mean observations we remove the over-land and over-polar region observations from the center plot. The right hand plot shows the mean observed BT1231 from the $1^\circ \times 1^\circ$ grid from the uniform/clear sky filter as a function of latitude, compared to the $1^\circ \times 1^\circ$ grid from the Q0.90 scenes. The difference between the uniform/clear versus Q0.90 average is within about $0.25 \text{ K} \pm 1 \text{ K}$ across the southern tropics to the northern midlatitudes, though the bias rises to about 1 K by about -50°S . We consider this an acceptable difference, as we could tune the thresholds for the uniform/clear filter to, for example, change the areal coverage and/or number of clear scenes and hence comparisons to the Q0.90 scenes.

The results presented in this section have been checked for robustness, using other 16 day intervals spanning the four seasons. We conclude that for any 16 day timestep the radiances used in the Q0.90 average (a) produces almost complete spatial coverage of the Earth, (b) selects scenes whose average BT1231 is very close to the average BT1231 from scenes selected using an uniform/clear filter (c) trends from that quantile typically differ by less than $\pm 0.002 \text{ K yr}^{-1}$ from the other quantiles and (d) this selection produces spectral trends which compare well against those obtained from the quality assured binned AIRS CCR data record (Manning, 2022), and reinforces the notion that nominally clear scenes are filtered through by our quantile based selector. Together these imply the Q0.90 average is an acceptable proxy for “clear scenes.” For the remainder of the paper we therefore consider Q0.90 as consisting of nominally clear observations whose BT1231 lies between the 90th quantile and hottest observation. Our retrievals using this Q0.90 \rightarrow Q1.00 averaged observational data set (shortened to Q0.90) is referred to as AIRS_RT in what follows.

3.2. Computing Observed Trends in the Selected Q0.90 Quantile of Radiances

Having selected the Q0.90 observations, for each tile the average radiance per 16 day interval is computed. With two 16 day periods not available (Aqua platform or AIRS shutdowns during, e.g., solar flare events) this gives a total of 457 time steps over 20 years. Anomalies are formed from this time series, and then deseasonalized to give the spectral radiance trends and error estimates (Strow & DeSouza-Machado, 2020) using *Matlab robustfit*:

$$r_{\text{observations}}^{16 \text{ days}}(t) \sim r_{\text{fit}}(t) = r_o + a_1 t + \sum_{i=1}^4 c_i \sin(n2\pi t + \phi_i) \quad (2)$$

with a_1 and its associated uncertainty, both converted to brightness temperature (BT), being the trends in K yr^{-1} . Using sub-harmonics in the fit did not produce any noticeable change in the AIRS_RT retrievals (described below). The uncertainty includes a correction for the lag-1 autocorrelation in the residual time series (B. Santer et al., 2000). Further details about noise and uncertainty of the time series are found in Appendix A.

The left panel of Figure 3 shows the globally averaged spectral observations for the five quantiles mentioned above, averaged over 20 years (September 2002–August 2022) of descending (nighttime) orbit observations. We note the spectra in most of the plots in this section are weighted by the $\cos(\text{latitude})$ of the tiles, unless otherwise stated. In addition we only show the $640\text{--}1640 \text{ cm}^{-1}$ region, and ignore the shortwave $2050\text{--}2750 \text{ cm}^{-1}$ region since the AIRS SW channels are drifting relative to the LW (Strow & DeSouza-Machado, 2020). Spectral averages constructed from Figure 1 would have this same behavior, namely that in the window region the mean spectrum of observations populating the warmer quantiles (Q0.80, Q0.90, Q0.95, and Q0.97) as defined in Equation 1 are on the order of a Kelvin apart, and have about half/quarter that difference in the optically thicker regions dominated by H_2O and/or CO_2 absorption, respectively.

The right hand panel of Figure 3 shows (top) the trends and (bottom) the 2σ trend uncertainties for these quantiles, in K yr^{-1} . We emphasize that the top right panel shows that the spectral trends for the quantiles lie almost on top of each other; the difference between the Q0.50 and other trends is at most about $+0.003 \text{ K yr}^{-1}$ (out of a 0.02 K yr^{-1} signal) in the window region (and about $+0.0045 \text{ K yr}^{-1}$ in the troposphere temperature sounding channels), or less than 10%. Similarly the largest trend uncertainty in the bottom panel is for Q0.50. This implies that clouds effects in the infrared produce the largest variability (blue curve). Globally on average for the infrared the spectral trends for all quantiles, ranging from clearest (Q0.97) to all-sky (Q0.50) are very similar, but differences are seen

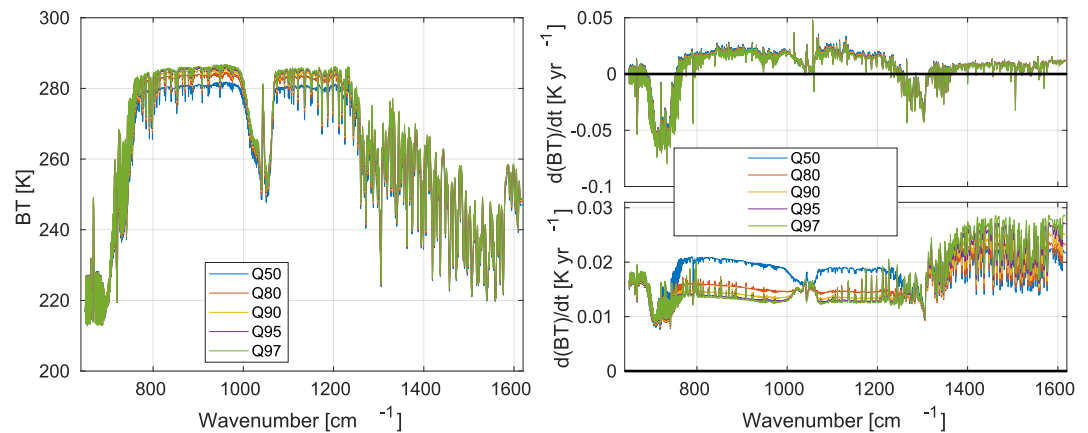


Figure 3. Twenty year trends from different observation quantiles. The left hand panel shows the mean globally averaged BT observations (in Kelvin) from 20 years of AIRS observations, for quantiles Q0.50, 0.80, 0.90, 0.95, and 0.97 as described in the text. The right hand panel shows (top) the globally averaged trends for those different quantiles and (bottom) the spectral uncertainty in the trends (both in K yr^{-1}). The nighttime (descending) trends are shown in these plots.

on regional scales. This implies the $+0.022 \text{ K yr}^{-1}$ window region trends are dominated by surface temperatures changes and to a lesser extent by water vapor changes.

X. Huang et al. (2023); Raghuraman et al. (2023) and our work all show, either in radiance or OLR space, (a) the increased observed radiance in the window channels, due to surface temperature increases (b) the $\approx -0.06 \text{ K yr}^{-1}$ decrease in BT in the $700\text{--}750 \text{ cm}^{-1}$ troposphere sounding region, which is due to a combination of the CO_2 amounts/optical depth rises leading to atmospheric emission from higher altitudes/lower temperatures together with atmospheric temperature increases (shown later in this paper to be between $+0.01$ and $+0.02 \text{ K yr}^{-1}$); (c) increases in the $1350\text{--}1640 \text{ cm}^{-1}$ free troposphere water vapor sounding region and (d) the $1280\text{--}1340 \text{ cm}^{-1}$ decreases are due to CH_4 increases.

Also of interest are the trends in the stratosphere ($650\text{--}700 \text{ cm}^{-1}$) changes which consists of a stratospheric cooling signal (negative) and emission higher up due to increased CO_2 ; combining to give a net zero effect over 20 years, also seen in (Raghuraman et al., 2023). The H_2O signal is evident in the $1400\text{--}1625 \text{ cm}^{-1}$ region, and is only slightly positive; in other words, increasing temperatures have led to increased atmospheric amounts of H_2O , and the water vapor feedback has reduced the amount of outgoing flux in that region. By extension, this can also be expected to have happened in Far Infrared ($10\text{--}650 \text{ cm}^{-1}$) spectral regions affected by water vapor, but cannot be wholly confirmed as current sounders do not make direct measurements in that region. In the near future it is anticipated the Far Infrared Outgoing Radiation Understanding and Monitoring (FORUM) mission (Palchetti et al., 2020) will provide observations to fill in this important observation gap.

4. Spectral Closure: Comparisons Between Observed and Simulated Spectral Trends

AIRS radiances have been shown to have very low drifts (equivalent to less than 0.002 K/year) and are therefore suitable for climate studies (Strow & DeSouza-Machado, 2020). Here we present the comparisons in radiance spectral trend space, by using the spectral closure method to assess monthly thermodynamic output from reanalysis and/or L3 retrieved products (see e.g., X. Huang et al., 2023). This is accomplished by geolocating the entire 20 year monthly reanalysis and L3 retrieved surface temperature, air temperature, water vapor and ozone fields for all 72×64 tiles. We also include realistic column linearly-increasing-with time mixing ratios for CO_2 , CH_4 , and N_2O as well as land or ocean surface emissivity co-located to tile centers together with view angles of about 22° , which is the average view angle of the tiled observations. The geophysical fields are then converted to spectral radiances by running through the SARTA fast model (Strow, Hannon, DeSouza-Machado et al., 2003). Finally, spectral radiance trends are computed from the time series of (clear sky) spectral radiances using Equation 2. This spectral closure, namely, the conversion of L3 retrieval and reanalysis monthly data to a radiance time series using an accurate radiative transfer algorithm, and then deseasonalized and trended, provides a

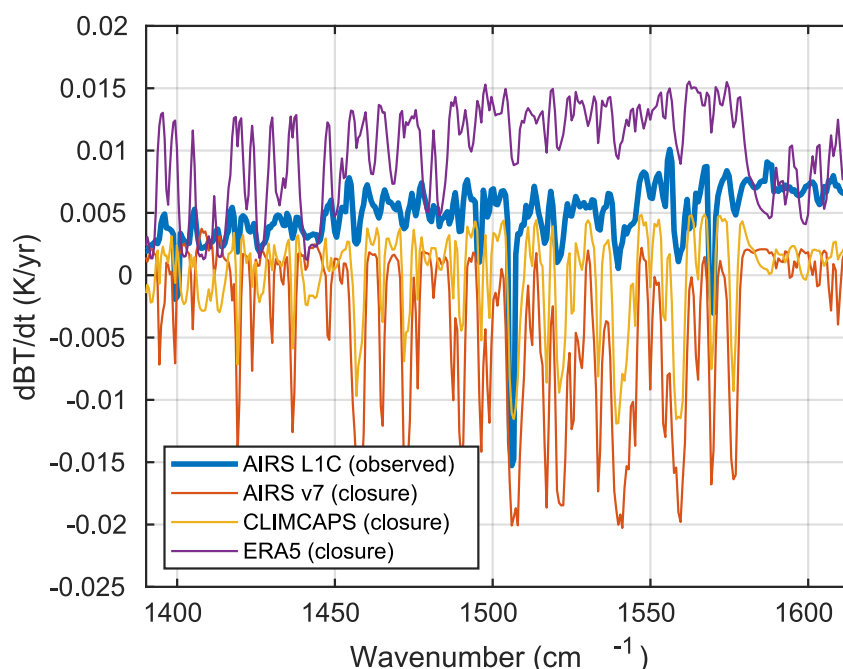


Figure 4. Globally averaged spectral trends (in K yr^{-1}) for the $6.7 \mu\text{m}$ ($1400\text{--}1650 \text{ cm}^{-1}$) free troposphere water vapor sounding region, as a function of wavenumber (cm^{-1}). AIRS L1C observations (blue) are compared to spectral closure from the standard monthly AIRS L3 retrievals (red) and CLIMCAPS L3 retrievals (yellow) and from monthly ERA5 simulations (purple). Nighttime AIRS overpasses are used in this plot. The reconstructed AIRS_RT trends very closely match the AIRS L1C observations and are not shown here.

rigorous check of their accuracy against the observed trends from the very stable AIRS instrument, independent of any AIRS_RT retrieval errors.

Here we select two examples to illustrate differences (in spectral space) between the five data sets we use in this paper. First, we study spectral trends in the water vapor sounding region. Water vapor is highly variable in space and time, and the typical ± 90 min difference between observation and forecast leads to noticeable differences between L2 water vapor retrievals compared to Numerical Weather Prediction (NWP) or reanalysis forecasts, when considered locally and at a particular observation time. However, this will not affect the water vapor trends we show in this paper since atmospheric water vapor timescale is on the order of about a week to 10 days (van der Ent & Tuinenburg, 2017), and we are also considering data points averaged over 16 days. Figure 4 show the globally averaged brightness temperature trends (in K yr^{-1}) in the $1350\text{--}1650 \text{ cm}^{-1}$ water vapor sounding region, for the nighttime (descending) AIRS overpasses. The blue curve shows the trends from the AIRS observations used in this paper, while spectral trends constructed from the AIRS L3/CLIMCAPS L3 retrievals are in red/yellow and the ERA5 geophysical output fields are in purple. The AIRS observations and ERA5 constructed spectral trends are positive in this region, while the trends from the AIRS L3 and CLIMCAPS L3 retrieved products are obviously different, being negative in this water vapor sounding region. The subtle differences in these spectral trends arise from differences in the geophysical trends between observations and the models themselves, and will be addressed in Sections 7.3 and 7.4 of the text.

Second, we focus on comparing zonally averaged spectral trends between AIRS observations and ERA5 simulations. Figure 5 shows the AIRS observed Q0.90 (nominally clear) descending (night) zonally averaged results in K yr^{-1} in the left panel, and the zonally averaged simulated clearsky (without clouds) spectral trends (also in K yr^{-1}) from monthly ERA5 fields in the right panel. The center panel shows the spectral trend uncertainties from the observations, also in K yr^{-1} . In the following sections we derive geophysical trends from the observed AIRS L1C spectral trends, and compare against reanalysis and L3 retrieval fields. The similarities/differences in geophysical trends between observations and models/operational data can be partially understood from the similarities/differences in the spectral trends. For example, the H_2O sounding region ($1350\text{--}1600 \text{ cm}^{-1}$) of the left and right panels of Figure 5 shows roughly similar (positive) spectral trends in the tropics and mid-latitudes;

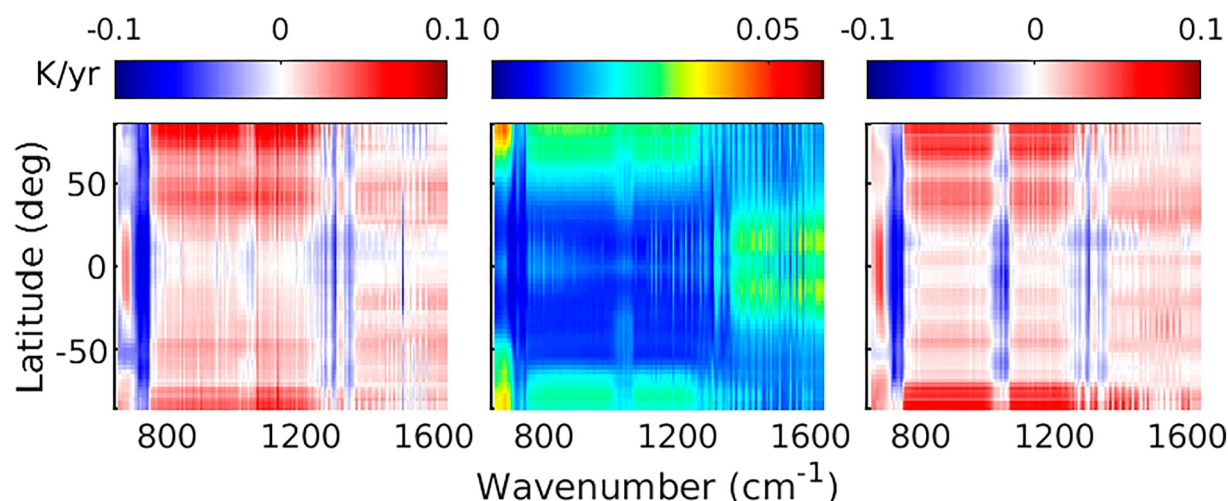


Figure 5. Twenty year zonally averaged spectral brightness temperature trends (color bars in K yr^{-1}) for nighttime (left) AIRS Q0.90 observations and (right) clear sky simulations using ERA5 monthly geophysical fields. The center panel shows the AIRS Q0.90 spectral uncertainties (color bar also in K yr^{-1}). Realistic linear trends of CO_2 , CH_4 , and N_2O were included in the ERA5 simulations, while the O_3 trends in ERA5 are from the reanalysis itself. Horizontal axes are in wavenumbers (cm^{-1}) while vertical axes are in degrees latitude.

there are some slight differences in the high altitude channels ($1450\text{--}1550\text{ cm}^{-1}$ region). The following sections will also demonstrated how these spectral differences translate to subtle differences in the geophysical trends. Observations and simulations both have positive $\text{dB T}/\text{dt}$ in the $800\text{--}960, 1150\text{--}1250\text{ cm}^{-1}$ region, indicating surface warming; however, the ERA5 simulation show more warming in the southern polar regions than do the AIRS observations. Note the mean warming in the tropics for both observations and ERA5 simulations is less than that in the mid-latitudes, and the polar regions show the largest overall change in brightness temperature in the window region. Large differences are seen in the $10\text{ }\mu\text{m}$ (1000 cm^{-1}) O_3 sounding region, which are not surprising since ozone assimilation is not a primary goal of ECMWF assimilation; here we do not address these as we focus on the changes to the moist thermodynamic state. The window region trends computed using the ERA5 geophysical fields are more positive in the Southern Polar region. Conversely the $640\text{--}700\text{ cm}^{-1}$ spectral region is positive, especially in the tropics; however, the observations show a net cooling trend away from the tropics, compared to the ERA simulations. This demonstrates the importance of the reanalysis/L3 geophysical \rightarrow spectral trend comparisons, given the accuracy of the AIRS observations.

5. Testing the Variability of Representative Points From Reanalysis

Each 16 day $3^\circ \times 5^\circ$ tile contains $\sim 12,000$ observations, resulting in about 600 daytime and 600 nighttime observations averaged for each tile to produce the Q0.90 observational data set per timestep. Conversely there are typically only ~ 240 monthly ERA5 0.25° points per $3^\circ \times 5^\circ$ tile; for 1° resolution AIRS L3 and CLIMCAPS L3 operational retrievals there are even fewer (15) points per tile. The much fewer reanalysis or L3 points available monthly per tile leads to two choices for building geophysical time series from the reanalysis and L3 operational retrievals (a) using (or interpolating to) the grid cell closest to the center of each $3^\circ \times 5^\circ$ tile and (b) averaging all the data within any $3^\circ \times 5^\circ$ tile. Option (a) is straightforward for both surface and profile fields, while (b) is straightforward for surface temperature but much more computationally intensive for profiles due to inhomogeneous land surface pressures and reanalysis of sigma levels within a tile. A third option would involve (c) averaging over the 10% warmest simulated BT1231 from reanalysis or L3 retrievals; this would have very few points contributing to the average (10% of 240 or 15), and can realistically be explored only for the ERA5 reanalysis geophysical fields.

We compared the three above options for the ERA5 reanalysis fields. First we built complete sets of approximately 240 ERA5 surface temperature points per tile per month; at 0.25° resolution one of these is almost certainly at the tile center. From these monthly sets, we could either directly read the tile center temperature (our default), or compute the average surface temperature over each tile, or compute the average of the hottest 10% surface temperatures over each tile. This was done for all 20 years (240 monthly timesteps) after which the three

time series were trended. Over ocean the differences between all three sets of data were typically $-0.001 \pm 0.005 \text{ K yr}^{-1}$, while over land the differences were about $0.001 \pm 0.01 \text{ K yr}^{-1}$. This is to be compared to mean trends of about $0.014 \pm 0.02 \text{ K yr}^{-1}$ over ocean and $0.025 \pm 0.04 \text{ K yr}^{-1}$ over land: the spread of the ocean and land ERA5 surface temperature trends for the three methods, is much smaller than the mean trends. The percent differences over the 64×72 tiles were typically zero centered Gaussians of FWHM 10%. In a similar fashion we assessed the 37 level ERA5 reanalysis temperature $T(p)$ and specific humidity $Q(p)$ fields to see how the profile trends changed if we switched between the tile-center profile match and the profile average over a tile. Zonally averaged the percent difference in trends for both temperature and fractional specific humidity were roughly zero centered Gaussians with FWHM = 2.5% over the 64 latitude bins \times 37 profile levels. Averaging over all 64×72 tiles yielded profile percent differences that typically can be characterized as within $\pm 1.5\%$ in the 100–1000 mb range.

From this analysis, for the other data sets used in this manuscript, we chose to use (a) the mean over a tile for surface temperature trends since this is straightforward to do for a scalar quantity and (b) the center tile point for the profile trends since this is computationally easier than computing the mean profiles without significant loss of accuracy.

6. Geophysical Trend Retrieval Outline

6.1. Setting Up the Retrieval Problem

The observed clear sky spectral brightness temperature for a tile at any time t can be modeled as

$$BT(\nu, t) = f(X(t), \epsilon(\nu, t), \theta(t)) + NeDT_{retrieval}(\nu) \quad (3)$$

where the state vector $X(t)$ has the following five geophysical state parameters: (a) surface temperature (ST), (b) atmospheric temperature profile $T(z)$, (c) water vapor profile $WV(z)$, (d) ozone profile $O_3(z)$ (e) greenhouse gas forcings (GHG) due to CO_2 , CH_4 , and N_2O changing as a function of time t and $f(X(t), \epsilon, \theta, \nu)$ is the clear sky radiative transfer equation for channel center frequency ν . The spectral noise $NeDT_{retrieval}(\nu)$ varies with scene temperatures and on particulars of the retrieval algorithm. For single footprint retrievals using daily observations, the spectral noise $NeDT_{retrieval}(\nu)$ in a typical tropical “clear scene” is about 0.1 K in window region, increasing to about 1 K in the $15 \mu\text{m}$ temperature sounding channels and about 0.2 K in the $6.7 \mu\text{m}$ water vapor sounding region, and is usually larger for operational L2 retrievals which use cloud clearing. We parametrize the GHGs using single numbers (such as $\text{ppm}(t)$ for the CO_2 column), and include the AIRS orbit and viewing angle geometry θ and the surface emissivity $\epsilon(\nu)$, while we omit forward model and spectroscopy errors. We ignore cloud scattering as well as the spatial variation of the state parameters, emissivity and scan angle geometry within a tile. Linearizing the above equation about the time averaged profile, the relationship between the observed spectral trends and desired thermodynamic trends is given by

$$\frac{dBT(\nu)}{dt} = \frac{\partial f}{\partial X} \frac{d}{dt} \overline{X(t)} = K(\nu) \frac{d}{dt} \overline{X(t)} + K_{\text{emissivity}}(\nu) \frac{d}{dt} \overline{\epsilon(t)} \rightarrow K(\nu) \frac{d}{dt} \overline{X(t)} \quad (4)$$

where the matrix $K(\nu)$ is the thermodynamic Jacobian (surface temperature, air temperature and trace gases) and we ignore any orbit drifts (changes to θ), instrument changes (changes to $NeDT_{retrieval}(\nu)$) and surface emissivity ($\epsilon(\nu)$); the last assumption is investigated in a later section. The overbars on parameters X denote this is a time average (linear trend) that we are working with, and we have converted from radiances in Equation 2 to brightness temperatures in Equations 3 and 4.

6.2. Jacobian Calculations

For a typical clear sky tropical sky atmosphere, the $800\text{--}1200 \text{ cm}^{-1}$ window region has surface temperature (SKT) Jacobians which are about $+0.5$ to $+0.75 \text{ K}$ per degree SKT change and -0.75 to -0.25 K per 10% change in column water vapor. The spectral variability in these window region Jacobians is primarily due to reducing water continuum absorption as you move from the 800 cm^{-1} end to the 1200 cm^{-1} ; consequently the surface temperature Jacobians becomes closer to unity and the column water Jacobians become closer to zero as water vapor amount decreases (drier atmospheres in the mid-latitudes and polar regions). The hyperspectral channels

used in this work assist in partitioning these two competing changes (though not perfectly), which we validate against other data sets in this study. As seen in Figure 5 typical magnitudes of the spectral trends on the left hand side of Equation 4 are less than about 0.1 K per year. Equation 4 is in the usual inversion form $\delta y = K \delta x$, and the OEM solution used to solve the anomaly time series in Strow et al. (2021) is also used here. The noise term $NeDT_{retrieval}(\nu)$ for the trend retrievals is now the uncertainty that naturally arises from the inter-annual variability when doing the linear trend fitting and lag-1 autocorrelations used in Equation 2. Examples of typical noise values are shown in the bottom right hand panel of Figure 3.

ERA5 monthly geophysical fields at tile centers, together with time varying concentrations of GHG such as CO₂, were averaged over 20 years so Jacobians could be computed. The GHG concentrations were a latitude dependent increase of about 2.2 ppm yr⁻¹ for CO₂ derived from the CarbonTracker (Peters et al., 2007) (CarbonTracker CT-NRT.v2023-4, <http://carbontracker.noaa.gov>) data at 500 mb. Our pseudo-monochromatic line by line code kCARTA (De Souza-Machado et al., 2018, 2020) was used with these averaged profiles to produce accurate analytic Jacobians. The HITRAN 2020 line parameter database (Gordon & Rothman, 2022), together with MT-CKD 3.2 and CO₂,CH₄ line mixing from the LBLRTM suite of models (Clough et al., 2005) were used in the kCARTA optical depth database (De Souza-Machado et al., 2018). A 12 month geographical land-varying spectral emissivity database spanning 1 year from Zhou et al. (2011) was used, while ocean emissivity came from Masuda et al. (1988). The atmospheric temperature, water vapor and ozone profile Jacobians, and the surface temperature and column Jacobians for the GHG gases such as CO₂ and CH₄ and N₂O, were then convolved using the best estimate AIRS Spectral Response Functions (Strow, Hannon, Weiler, et al., 2003).

Tests done for this paper including satellite zenith changes, together with the results in Strow et al. (2021), established that Jacobians derived from MERRA2 versus ERA5 produced no significant differences in the context of retrieved trends or anomalies done for this paper, as the uncertainty in linear trends due to inter-annual variability dominates over any uncertainty (or differences between) reanalysis geophysical fields.

6.3. Optimal Estimation Retrieval: State Vector, Covariance Matrices, and A Priori

Using monthly ERA5 geophysical fields averaged over 20 years, for each of the 64 × 72 tiles we computed analytic Jacobians for the (vector) atmospheric thermodynamic variables fractional water vapor, fractional ozone and temperature together with (scalar) surface temperature. We retrieved fractional gas concentration trends $dfrac{X}/dt = 1/X_{avg}(z)dX_{avg}(z)/dt$ to keep all values in the state vector at about the same magnitude. A single iteration OEM retrieval is used to simultaneously solve for the geophysical parameter trends. As in Strow and DeSouza-Machado (2020) the geophysical OEM covariance uncertainty matrices are a combination of Tikonov and covariance regularization. The uncertainties for the covariance matrices were typically [0.1,0.25,0.45] K yr⁻¹ for the surface/tropospheric/stratospheric temperature trends, and [0.04/0.02] yr⁻¹ for the fractional tropospheric/stratospheric water vapor trends. Tikonov L1 regularization Rodgers (2000) also included, with the scalar factor multiplying this regularization corresponding to about 1/10 the covariance uncertainties. The spectral uncertainties used in the retrievals come from the above mentioned trend uncertainties. For completeness we note that a sequential trend retrieval produces very similar geophysical trends.

Here we emphasize four unique points about our geophysical trend retrievals, which distinguishes this approach from trends derived from other data sets. First the *a priori* trend state vector is zero ($dST/dt = dT(z)/dt = dQ(z)/dt = 0$) for all geophysical parameters, except for water vapor where we enforced constant (or slightly increasing) relative humidity as described below. This ensures traceability of our retrieval is straightforward especially wherever the AIRS instrument has sensitivity. For example, the 300–800 mb water vapor trend retrievals will be based on the observed data only, thereby insulating us from any possible *a priori* information from, for example, climatology or reanalysis, unlike the operational AIRS V7 or CLIMCAPS retrievals which use first guesses based on neural net and MERRA2, respectively.

Second the 15 μm region of Figure 5 shows a large spectral overlap signal (−0.06 K yr⁻¹) from the increasing CO₂, which is much larger than the expected atmospheric temperature trend (0.01–0.02 K yr⁻¹). These correlations make it difficult to jointly retrieve both temperature changes and changes in well mixed GHGs such as CO₂. We chose to focus on retrieving temperature changes only, by spectrally removing the effects of changing CO₂, CH₄, and N₂O GHG concentrations. This was done by using the GHG trends estimated from NOAA ESRL

CarbonTracker data multiplied by the appropriate GHG gas column Jacobian (CO_2 , N_2O and CH_4 and CFC11, CFC12) computed as described above using the averaged over 20 years ERA5 monthly profile for each tile.

Third instead of using all 100 layers described in the AIRS forward model (Strow, Hannon, DeSouza-Machado et al., 2003), we combine pairs of layers for a 50 atmospheric layer retrieval, as the AIRS radiances contain far fewer than 100 pieces of information (see e.g., De Souza-Machado et al., 2018; Maddy & Barnet, 2008).

Fourthly, modern hyperspectral infrared sounders have highest sensitivity to temperature and water vapor in the mid-tropopause; see for example, the averaging kernels in Irion et al. (2018). Using a zero fractional WV trends *a priori* at all levels, it was fairly straightforward to obtain fractional WV(*z*) trends close to those from the reanalysis data sets in the 300–850 mb region. In order to improve our results in the lowest layers, we enforced a constant relative humidity approximation, which is a well-known, expected behavior under global climate change (Sherwood et al., 2010; Soden & Held, 2006). This was done by ignoring the contribution due to water vapor changes in the observed BT1231 trend, and using it as an approximation for air temperature trend over ocean; this allows us to compute an estimate of how the water vapor would need to change

$$RH(T) = \frac{e}{e_{sat}(T)} \Rightarrow \delta(RH) = \frac{1}{e_{sat}(T)} \delta e - \frac{e}{e_{sat}^2(T)} \delta e_{sat}(T) = \frac{1}{e_{sat}(T)} \delta e - \frac{e}{e_{sat}(T)} \frac{L_v}{R_v} \frac{1}{T^2} \delta T \quad (5)$$

where $e, e_{sat}(T)$ are the vapor pressures and we used $e_{sat}(T) = e_{s0} e^{\frac{L_v}{R_v} (\frac{1}{T_0} - \frac{1}{T})}$ (where L_v, R_v are latent heat of vaporization and gas constant, respectively) to go from the expression in the center to the expression on the right. If we expect the change in RH to be zero then $\frac{\delta e}{e} = \frac{L_v}{R_v} \frac{\delta T}{T^2}$, where we can use $\delta T / \delta t \sim d/dt BT1231$ to approximate the *a priori* fractional vapor pressure rates (or *a priori* fractional water vapor rates) between surface and 850 mb, smoothly tailing to 0 in the upper atmosphere. Subsection 7.2 has a similar discussion on a proposed method to alleviate the lack of sensitivity to upper atmosphere water vapor. Our default results in this paper are from using the MLS *a priori*, unless otherwise stated.

6.4. Testing on Synthetic Trend Spectra Made From ERA5 Reanalysis Monthly Fields

We tested the retrieval code by using it on the simulated nighttime only ERA5 spectral trends, and compared to geophysical trends computed directly from the ERA5 reanalysis. Spot checks of the spatial correlations of ERA5 fractional water vapor and temperature trends versus the trends retrieved from synthetic spectra/our retrieval algorithm, peaked at 500 mb with correlations of about 0.9, compared to 800 mb correlations of 0.80 and 0.55 for temperature and fractional water vapor trends, respectively and 200 mb correlations of 0.89 and 0.69 for dT/dt , dWV_{frac}/dt . This is to be expected since a computation of the water vapor averaging kernels for infrared instruments for arbitrary atmospheric profiles typically shows they peak in the 300–850 mb range and decrease rapidly away from those regions; conversely the temperature averaging kernels stay relatively uniform through the free troposphere and above, though they also decrease close to the surface (see e.g., Irion et al., 2018; Smith & Barnet, 2020; Wu et al., 2023).

Figure 6 shows a sample set of results using nighttime ERA5 geophysical output converted to spectral trends as described above. The top panels (a) are always the atmospheric trends computed directly from the monthly ERA5 geophysical fields, while the bottom panels (b) are the atmospheric trends retrieved from the converted ERA5 spectral brightness temperature trends. The left most panel is the atmospheric temperature trend comparison (both in K yr^{-1}) while the rightmost panel is the fractional atmospheric water vapor trend comparison (in yr^{-1}).

It is evident from the figure that the tropospheric trends in the tropical and midlatitude regions are quite similar, and there are differences in the polar regions and stratospheric regions where the AIRS instrument has reduced sensitivity. The atmospheric and surface trends are shown in Table 1, divided into “all” (which is the entire ± 90 latitude range and 0–1000 mb vertical range) and “T/M” which is the tropical/midlatitude region, which is further reduced to 050–900 mb for air temperature and 300–800 mb for water vapor. “ERA5 direct” are trends computed directly from the geophysical fields, while “ERA5 spectral” are retrieved from the spectral trends.

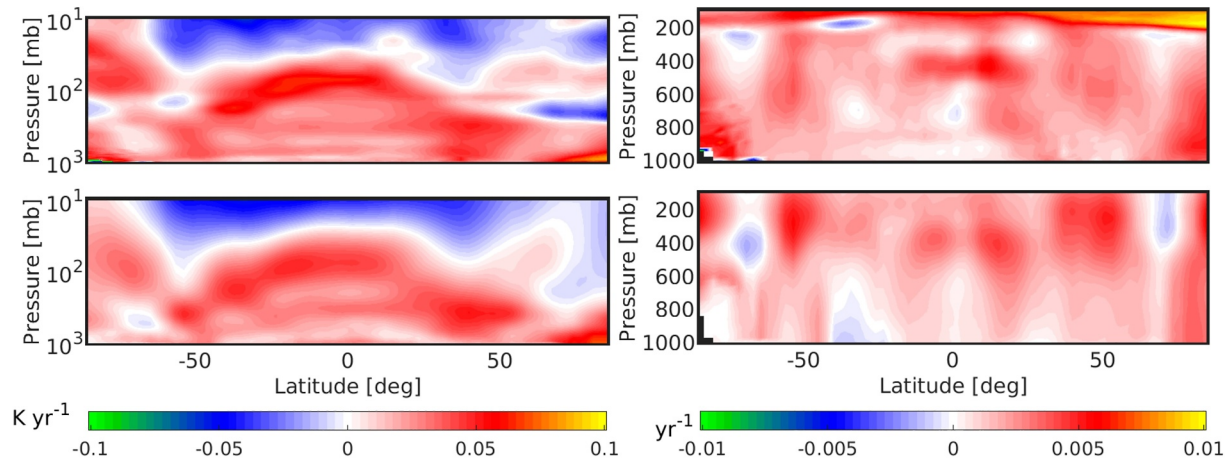


Figure 6. Comparing geophysical trends derived directly from ERA5 monthly nighttime fields (top) versus from the AIRS_RT retrieval applied to the ERA5 reconstructed spectral trends (bottom). The left hand panels are temperature trends (dT/dr) in $K\ yr^{-1}$ while the right hand panels are fractional water vapor trends ($dWVfrac/dr$) in yr^{-1} (as fractional water vapor has no units). Horizontal axis are all in latitude (deg) while vertical axis is in pressure (mb). Note the vertical axis is logarithmic for the temperature trends and linear for the water vapor trends.

6.5. Surface Emissivity Changes

Equation 3 explicitly includes the surface emissivity in the equation of radiative transfer; however, Equation 4 assumes this is unchanging. Here we rewrite Equation 4 as

$$\frac{d\overline{BT}(\nu)}{dt} - K_{emissivity}(\nu) \frac{d\overline{\epsilon(t)}}{dt} \rightarrow \frac{d\overline{BT}'(\nu)}{dt} = K(\nu) \frac{d\overline{X(t)}}{dt} \quad (6)$$

Ocean emissivity has a dependence on windspeed (Lin & Oey, 2020; Masuda et al., 1988) and other literature suggest wind speed increases of $+2.5\ cm\ s^{-1}\ yr^{-1}$ have occurred between 1993 and 2015 in the tropical Pacific, and smaller (or close to zero) values elsewhere. The monthly ERA5 $u10,v10$ 10 m speeds for the 20 year time period in this paper also showed the maximum absolute trend was $0.09\ m/s/year$ (over the Southern Ocean) while the global ocean mean and standard deviation were $0.006 \pm 0.022\ m\ s^{-1}\ yr^{-1}$; The emissivity changes over ocean using a $0.025\ m\ s^{-1}$ wind speed change are on average on the order of 1×10^{-6} per year in the thermal infrared window (or about $0.0003\ K\ yr^{-1}$ change in the window region); assuming the optical properties of water do not substantially change with the $\sim 0.02\ K$ increases seen in all the data sets considered in this paper, these very small emissivity changes due to windspeed changes are of no consequence.

We also estimate how the changing ocean temperatures would change the emissivity. Assuming no atmosphere, the radiance measured at the TOA is $r_0(\nu) = \epsilon(\nu)B(\nu, T_0)$ where T_0 is the temperature, ϵ is the emissivity and $B(\nu, T_0)$ is the Planck function. If the temperature is perturbed by δT then the radiances changes by an amount

Table 1

Cosine Weighted Air Temperature and Skin Temperature Trends (in $K\ yr^{-1}$), and Fractional Water Vapor Trends (in yr^{-1}), Together With Uncertainties

	dTz/dr $K\ yr^{-1}$ A SFC-TOA	dTz/dr $K\ yr^{-1}$ T/M 050–900 mb	$dSKT/dr$ $K\ yr^{-1}$ A	$dSKT/dr$ $K\ yr^{-1}$ T/M	$dfracWV/dr$ yr^{-1} A GND-TOA	$dfracWV/dr$ yr^{-1} T/M 300–800 mb
ERA5 direct	0.010 ± 0.038	0.029 ± 0.013	0.020 ± 0.035	0.018 ± 0.032	0.003 ± 0.002	0.002 ± 0.001
ERA5 spectral	0.004 ± 0.033	0.027 ± 0.012	0.019 ± 0.033	0.016 ± 0.029	0.001 ± 0.001	0.002 ± 0.001

Note. The “ERA5 direct” are directly from the ERA5 geophysical trends, while “ERA5 spectral” are trends retrieved from the converted ERA5 spectral trends.

$\delta r(\nu, T_0) = \epsilon(\nu) \frac{dB(\nu, T_0)}{dT} \delta T + B(\nu, T_0) \frac{d\epsilon(\nu, T_0)}{dT} \delta T$. The derivative of the Planck function is easily computed analytically. An estimate of the ocean emissivity change with temperature is $\sim 2 \times 10^{-4}$ per Kelvin, using the information in Nalli et al. (2022) and Newman et al. (2005). Inserting these numbers yields a BT change of $\sim 1.5 \times 10^{-3}$ K due to the change in emissivity, which is much smaller than the assumed 0.2 K ocean temperature change.

Land emissivity changes were estimated as follows. A global monthly mean emissivity database, the Combined ASTER and MODIS Emissivity over Land (CAMEL v003) has recently been released (Borbas et al., 2018). We matched the tile centers to the database for the 20 \times 12 months spanning our 2002/09–2022/08 time period, and computed the emissivity trends over land; the results (not shown here) were on the order of -1×10^{-4} and $+3 \times 10^{-4}$ in the 800–960 cm^{-1} and 1100–1250 cm^{-1} regions, respectively, averaged over the land observations. For each tile the $K_{\text{emissivity}}(\nu) \frac{d}{dt} \epsilon(t)$ term was estimated by running SARTA with the default emissivity, then differencing with the SARTA output obtained when the emissivity trends were added on. Averaged over the planet, the spectral changes arising from these emissivity changes were much smaller than the spectral trends seen in Figure 3, about -0.001 K yr^{-1} between 800 and 960 cm^{-1} and about $+0.002 \text{ K yr}^{-1}$ on the 1100–1250 cm^{-1} region (which we do not use in our retrieval, since many of the channels are synthetic and the real channels are drifting Strow et al. (2021)). The land only results were roughly three times these magnitudes. Using these emissivity Jacobians on the left hand side of Equation 6 and running the retrieval on the adjusted spectral trends over land, resulted in about at most 0.01 K increases to the zonally averaged surface temperature changes over land; zonally averaged these largest differences were at about 40°N to 60°N and -25°S to $+15^\circ\text{N}$, due to emissivity decreases; the 20°N to $+35^\circ\text{N}$ region which included the Sahara and swathes of Asia, had emissivity increases but the averaged-over-land temperature decreases were small, as there were offsetting emissivity increases in other land areas at the same latitudes. We did not pursue the impact of these emissivity changes further as the CAMEL database is affected by the stability of the MODIS data, and our results below will not include accounting for changes in land emissivity.

7. Geophysical Trends From Observational AIRS_RT Compared Against Trends From Legacy Reanalysis and L3 Retrieval Products

The trends retrieved in the previous section using simulated radiance trends show that the retrieval package is working as expected. Here we apply our retrieval to observed AIRS L1C radiance trends and compare the retrieved AIRS_RT geophysical trends to those computed directly from the ERA5/MERRA2 geophysical fields and AIRS L3/CLIMCAPS L3 retrieval products. We will have an expectation that since the simulated radiance trends had no noise added to them, the uncertainty in the spectral rates was lower than the actual observed spectral uncertainty; this will lead to larger uncertainties and/or errors in our retrieval using observed radiance trends.

Most of the comparisons against reanalysis geophysical fields and L3 retrieval products will be made in the context of averages over the descending/night (N) and ascending/day (D) observations since the MERRA2 (and GISS) data sets are only available as a D/N average; we show a few of the D–N differences in Appendix B. The results are shown in the order of surface/column trends (surface temperature and column water), followed by zonal averages of the atmospheric temperature and fractional water vapor trends. We also refer the reader to Section 4 which presents an interpretation of these geophysical trend comparisons, using trends in radiance spectral space.

7.1. Skin Temperature Trends

There are typically multiple (window) channels that are sensitive to a surface pressure, meaning the radiances typically have more information content for the surface temperature (assuming the surface emissivity is well known and there are no clouds) rather than, for example, air temperature. Figure 7 shows the diurnally averaged day/night (D/N) surface temperature trends from 6 data sets: AIRS_RT observations, AIRS L3, CLIMCAPS L3, ERA5, MERRA2, and NASA GISTEMP. AIRS_RT shows an overall global warming of $+0.021 \text{ K yr}^{-1}$; the cooling trends include the tropical eastern Pacific and south of Greenland and tropical northern Atlantic. The rest of the data sets also show similar patterns of cooling in the N. Atlantic Ocean, warming over the Arctic and some degree of cooling over the Antarctic Ice Shelf/Southern Ocean as does AIRS_RT. The AIRS v7 L3 operational retrieval shows some cooling over Central Africa and the Amazon not seen in the AIRS_RT trends, where one

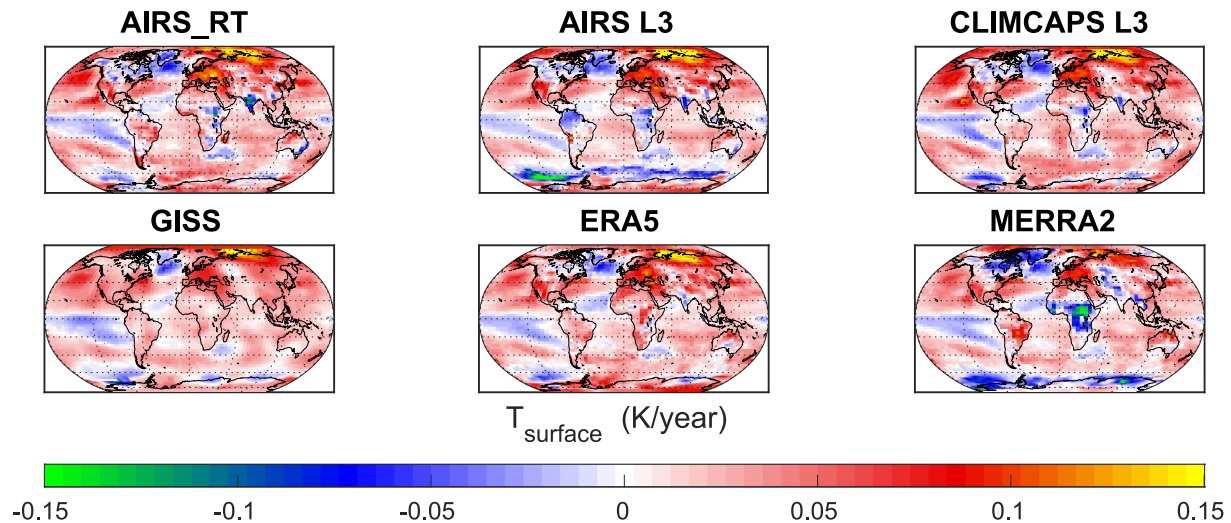


Figure 7. Surface temperature trends $dSKT/dt$ averaged over day and night for AIRS_RT, and separately fitting the monthly data in ERA5, MERRA2, AIRS L3, CLIMCAPS L3, and GISS. The horizontal and vertical axis are longitude and latitude. Color bar units are in $K\ yr^{-1}$.

could expect Deep Convective Clouds and possible cloud clearing issues. We also point out the AIRS L3 retrieval product has many missing values off the western coasts of N. and S. America, due to cloud clearing issues. MERRA2 shows significant cooling trends over C. Africa and near the Antarctic Ice Shelf. Of note here is that although CLIMCAPS uses MERRA2 as its first guess, their surface temperature trends are not similar, especially around the Antarctic where MERRA2 shows strong cooling trends. Over the ocean GISS shows similar trends to what AIRS_RT trends show. An earlier study of Land Surface Temperatures between 2003 and 2017 using MODIS (Prakash & Norouzi, 2020) shows very similar large daytime cooling trends over parts of central and western Indian subcontinent that we see from our retrieval as well as directly from the BT1231 channel trends; for tiles that straddle both ocean and land the quantile method picks up the hottest observations, which especially during summer are mostly over the Indian subcontinent. For these reasons we also have confidence in our retrieved cooling trends over for example, daytime continental Central/Eastern Africa, which are different from the other 4 day/night data sets.

The spatial correlations between AIRS_RT retrieved rates and the various data sets is shown in Table 2 while the cosine weighted skin temperature trends are shown in Table 3. By adding in the uncertainty in the trends for any of the individual models or data sets, and then doing the cosine weighting, we estimate uncertainties of about $\pm 0.015\ K\ yr^{-1}$ for “ALL”; the uncertainties for “OCEAN” are typically about 2/3 of that value, and for “LAND” are about 4/3 of that value. We emphasize here that we use reanalysis geophysical fields and L3 operational retrieval products averaged over a tile when computing their trends, while the AIRS_RT uses the hottest 10% of “clear” observations (Strow & DeSouza-Machado, 2020); showed that the tropical retrieved surface temperature trends and anomalies over ocean correlated very well with those from the ERA-I Sea Surface Temperature data set.

A notable outlier in this group is the MERRA2 trends, especially over land and the Southern Ocean which are noticeably negative (blue) compared to the other data sets; the agreement with tropical and mid-latitude oceans is much better. As noted earlier, the MERRA2 monthly trends come from a combination day/night data set that was downloaded, which as seen in Figure 7 consists of trends that are both positive and negative, combining to get a closer-to-zero global weighted trend. In addition MERRA2 is the only one of the six that (a) does not have the

extreme $+0.15\ K\ yr^{-1}$ warming in the northern polar region and (b) shows substantially more cooling in the Central African area. Using ERA5 monthly data, we devised a test similar to the one mentioned in Section 5 to determine if the differences between MERRA2 and ERA5 surface temperature trends could be due to the temporal sampling (once for MERRA2 vs. eight times for ERA5). For each month we matched the eight ERA5 timesteps available per month to the tile centers and then averaged the surface temperatures per

Table 2
Correlations of Average (Nighttime, Daytime) Retrieved Skin Temperature Trends From AIRS_RT, Versus Trends From Models/Products

ERA5	MERRA2	AIRSL3	CLIMCAPSL3	GISS
0.78	0.62	0.80	0.90	0.77

Table 3

Cosine Weighted Skin Temperature Trends (in $K yr^{-1}$); Uncertainties Are on the Order of $\pm 0.015 K yr^{-1}$ as Explained in the Text

SKT trend $K yr^{-1}$	AIRS_RT	AIRS	CLIMCAPS	ERA5	MERRA2	GISS
ALL	0.021	0.015	0.022	0.022	0.012	0.021
TROPICS	0.013	0.011	0.014	0.015	0.010	0.015
MIDLATS	0.028	0.018	0.029	0.027	0.020	0.026
POLAR	0.032	0.025	0.033	0.038	−0.004	0.028
OCEAN	0.019	0.012	0.021	0.017	0.012	0.017
LAND	0.025	0.024	0.026	0.035	0.010	0.030

month; the ensuing geophysical time series was then trended. The day/night ERA5 average of Figure 7 was compared to these trends; of note are (a) we did not see the cooling in Africa and near the Antarctic that is seen in MERRA2 and (b) the main differences between the 1.30 a.m./1.30 p.m. average in the bottom middle (ERA5) panel were over land (all 5 continents); the histograms of the differences showed the peak was typically close to $0 K yr^{-1}$, but the widths over land were about $\pm 0.02 K yr^{-1}$ or less (compared to $\pm 0.005 K yr^{-1}$ over ocean). Trends from AIRS L3 retrievals and MERRA2 geophysical fields show cooling in the Southern Ocean; we note that although MERRA2 is the *a priori* for CLIMCAPS L3, their trends are different that those from MERRA2; in fact AIRS_RT shows the closest correlation to the CLIMCAPS L3 retrieval product trends. The AIRS L3 trends in the Southern Ocean region could arise because of problems identifying ice during the L2 retrieval (private communication: Evan Manning (JPL) and John Blaisdell (NASA GSFC)) though the MERRA2 trends also show significant cooling in that region, where few surface observations from buoys poleward of 60° exist to help resolve these differences (see e.g., Figure 10 in Haiden et al., 2018).

Figure 8 shows the zonally averaged total (land + ocean) and ocean only surface temperature trends. The equator to midlatitude ocean trends are almost linear for all data sets, with the slope for the northern hemisphere being about double that of the southern hemisphere (roughly $0.001 K yr^{-1}$ per deg latitude). Again, focusing on the right hand plot, the AIRS L3 trends are negative in the Southern Ocean regions, compared to the other three data sets, due to the cooling trends around the Antarctic continent shown earlier, but then agrees with most of the other data sets over the Antarctic; the MERRA2 trends significantly differ between $-90^\circ S$ and $-50^\circ S$. MERRA2 and ERA5 also show slightly smaller warming trends in the Northern Polar, compared to the three AIRS observation-based data sets.

We point out that the trends seen in Figure 7 vary noticeably at more local, regional levels and furthermore this spatial variation can differ between daytime and nighttime, evident in Figure B1 of Appendix B, and that the trends derived from observations (AIRS_RT, CLIMCAPS L3, and AIRS L3) had larger differences than ERA5. Discussing the possible causes is outside the scope of the paper.

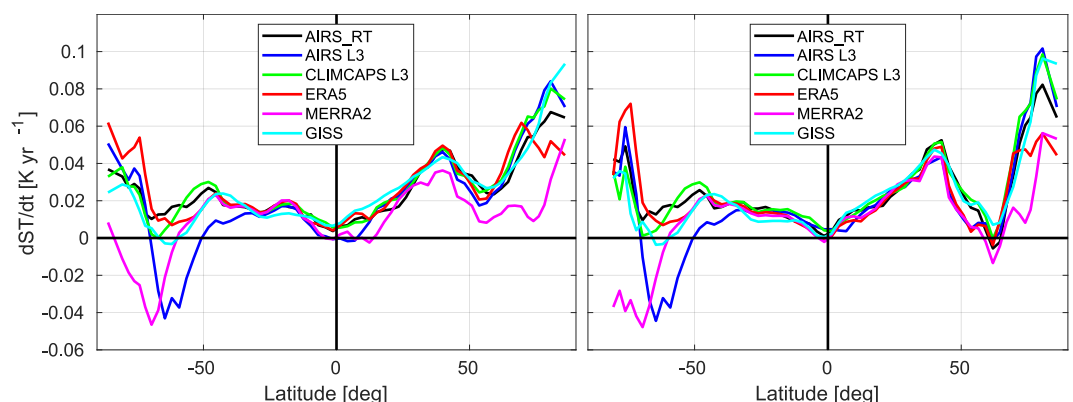


Figure 8. Zonally averaged surface temperature trends for (left) sum of ocean and land point and (right) ocean only. The vertical units are $K yr^{-1}$ while the horizontal axis are degrees of latitude.

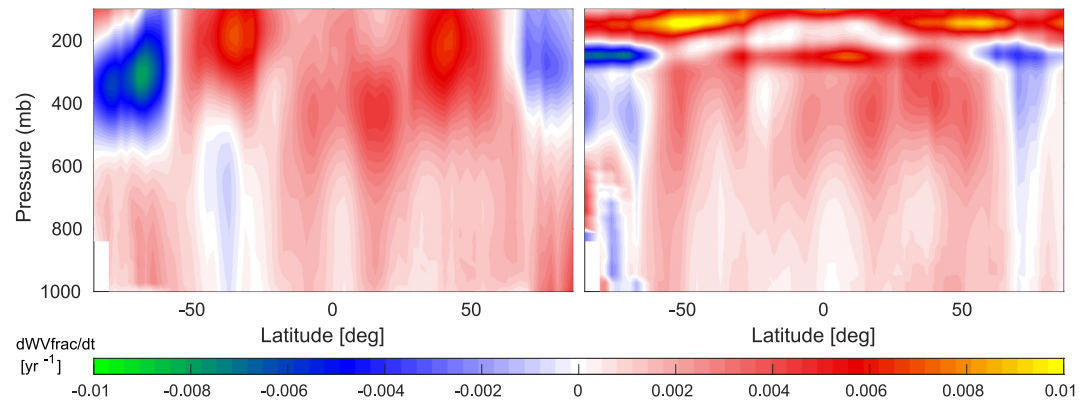


Figure 9. $dWVfrac/dt$ (left) without and (right) with MLS *a priori* in the upper atmosphere. The vertical axis are pressure (in mb), the horizontal axis are latitude (in degrees) while the color bar is in yr^{-1} (fractional water vapor has no units).

7.2. Addition of Microwave Limb Sounder Water Vapor A Priori

The Microwave Limb Sounder (MLS), on board NASA's Aura platform, flies about 15 min behind AIRS on the same orbit. It is designed for sounding of the atmosphere above 300 mb. We computed water vapor trends from the L3 operational retrievals produced for that instrument (above 300 mb) and used them as an *a priori* for the AIRS_RT retrieval.

Figure 9 shows the retrieved fractional water vapor trends when the *a priori* trend in the upper atmosphere in the left and right panels were zero, or used MLS trends, respectively. One sees that the additional information brought in by the instrument sensitive to upper troposphere humidity, significantly changes the water vapor sounding especially in the polar region by moving toward the MERRA2 and ERA5 fractional water vapor trends seen in Figure 12. We note that the other related results shown in this paper also use the MLS *a priori*.

7.3. Column Water Vapor Trends

Column water is dominated by water vapor amounts close to the surface and the column vapor trends thus provide an assessment of the water vapor retrieval quality in the lower atmosphere. The water vapor information in the lowest layers is best retrieved using the weak water lines in the thermal infrared region. As noted earlier this part of the retrieval is significantly complicated by the simultaneous presence of nonzero surface temperature, air

temperature and water vapor Jacobians in this spectral region, meaning the AIRS instrument has much reduced sensitivity to the water vapor amounts in these lowest layers. In addition the changing concentration of very minor gases such as CFC-11 and CFC-12 (Strow & DeSouza-Machado, 2020) are quite evident in the spectral trends, further complicating the water vapor trend retrieval for the lowest layers.

Figure 10 shows the zonally averaged column water vapor trends; not shown are the error bars which are on the order of ± 0.005 mm/year. AIRS_RT is from our retrievals while the rest are directly from the reanalysis or L3 operational retrieval fields. Close examination shows the CLIMCAPS L3 column water trend is nearly identical to the MERRA2 trend, as is also seen in lower atmosphere water vapor trends shown later in Figure 12. Conversely the column water vapor trends for AIRS L3 are negative in the lower troposphere in the midlatitudes and tropics, which is not to be expected given that the surface temperature trends are positive. AIRS_RT is slightly smaller but nominally agrees with ERA5 and MERRA2 in the tropics and midlatitudes, but is smaller than either in the northern polar regions. A reduced rate for AIRS_RT is additionally seen in the 0–50°N latitudes, where there is a larger fraction of land (for which we do not use the assumption of constant relative humidity) compared to the Southern Hemisphere. Screening out the tiles over land

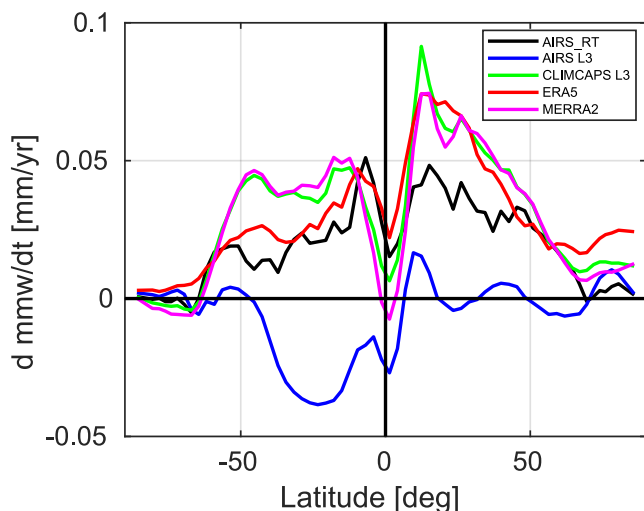


Figure 10. Zonally averaged column water vapor trends for AIRS_RT, AIRS L3, CLIMCAPS L3, ERA5, and MERRA2. Vertical units are in $MMW\ yr^{-1}$ while the horizontal axis are in degrees latitude.

Table 4
Column Water Trends Based on OMI Observations (16 Years) and AIRS_RT, ERA5, and MERRA2 (20 Years)

DATASET	OMI	AIRS_RT	ERA5	MERRA2	AIRS L3	CLIMCAPS L3
mm yr ⁻¹	16 years	20 years	20 years	20 years	20 years	20 years
GLOBAL (cosine average)	0.051	0.021	0.035	0.036	−0.009	0.038
TROPICAL	0.083	0.028	0.047	0.042	−0.015	0.045

Note. The units are in mm yr⁻¹; the uncertainties are on the order of 0.1 mm yr⁻¹ for OMI and AIRS_RT, and half that for ERA5 and MERRA2, and AIRS L3 and CLIMCAPS L3.

slightly improves the agreement between reanalysis (ERA5, MERRA2) versus AIRS_RT column water trends. Examination of the spectral trends in the window region does not shed any more insight into the differences, as the observation spectral trends and reanalysis reconstructed trends are very similar and we are fitting the observed trends. The magnitudes and patterns look similar to the 2005–2021 column water trends shown in Borger et al. (2022), which were derived using observations from the Ozone Monitoring Instrument (OMI). We point out their 16 year zonally averaged trends look similar to the 20 year ERA5 zonally averaged column water trends between −60°S and −10°S, but become almost a factor of 2 larger between −10°S and +40°N; the zonally averaged OMI 16 year trends are negative in the polar regions. The column water trends are summarized in Table 4.

D/N differences (not shown) for AIRS_RT were on the order of ±0.005 mm yr⁻¹ (with daytime trends being smaller over land), for AIRS L3 were on the order of ±0.01 mm yr⁻¹ or more (with larger values happening over the daytime tropical oceans), while that for ERA5 and CLIMCAPS L3 were typically on the order of ±0.03 mm yr⁻¹ or less.

7.4. Zonal Atmospheric Temperature and Water Vapor Trends

Figure 11 shows the zonally averaged atmospheric temperature trends from five of the data sets in Figures 7 and 10 above. In the troposphere the AIRS_RT retrievals show the same general features as the trends from ERA5, though they begin to diverge in the stratosphere and especially above that. In particular AIRS_RT does not show warming in the Southern Polar stratosphere; we have separately looked into seasonal trends and noted that our retrieved September/October/November temperature trends in the upper atmospheric Southern Polar regions are on the order of −0.12 K yr⁻¹, possibly leading to an overall no net heating/cooling for the annual trends. We highlight that our zonally averaged atmospheric trend results are smoother than those of the other data sets, while the other sets have noticeable discontinuities that may not be physical under the thermodynamics or fluid dynamics frameworks. In addition the reanalysis models ingest many observational data sets, while the L2/L3 operational retrieval products are influenced by the *a priori*. In addition we point out that both our results and AIRS v7 L3 retrievals show a hint of cooling over the tropical surfaces. Note that CLIMCAPS is initialized by MERRA2, and their temperature trends are quite similar. AIRS v7 looks similar to AIRS_RT except in the tropics where it almost has cooling in the lower troposphere and much more warming in the lower stratosphere. The correlations between AIRS_RT and the [AIRS L3, CLIMCAPS L3, MERRA2, ERA5] temperature trends of Figure 11 are [0.74, 0.65, 0.74, 0.72], respectively.

Figure 12 shows the zonally averaged atmospheric fractional water vapor trends ($d/dt WV(z,t)/\langle WV(z,t) \rangle$). The five panels are markedly different from one another. The AIRS_RT trends resemble those of ERA5 in the tropical troposphere, though we do not have drying in the lower tropical layers. Conversely, the trends in the Southern Polar derived from sounder observations (AIRS L3, CLIMCAPS L3 and AIRS_RT) show drying rather than wetting, though AIRS_RT is less than that of CLIMCAPS/MERRA2. AIRS_RT is an outlier in the upper polar atmosphere trends, as both the signals and the Jacobians are close to zero. Of some concern is a little bit of drying in the northern polar region, where there are low H₂O amounts leading to small Jacobians. CLIMCAPS v2 looks quite similar to the MERRA2 trends. AIRSv7 shows substantial drying in the lower troposphere, and considerable wetting in the upper troposphere, compared to any of the other data sets. Separate spectral closure studies using the AIRS v7 H₂O trend × the H₂O Jacobians derived above from ERA5 average profiles differ noticeably from the CCR trends from AIRS v7 in the 1300–1600 cm⁻¹ region, indicating there are inadequacies in the AIRS V7 water vapor retrievals. The correlations between AIRS_RT and the [AIRS L3, CLIMCAPS L3, MERRA2,

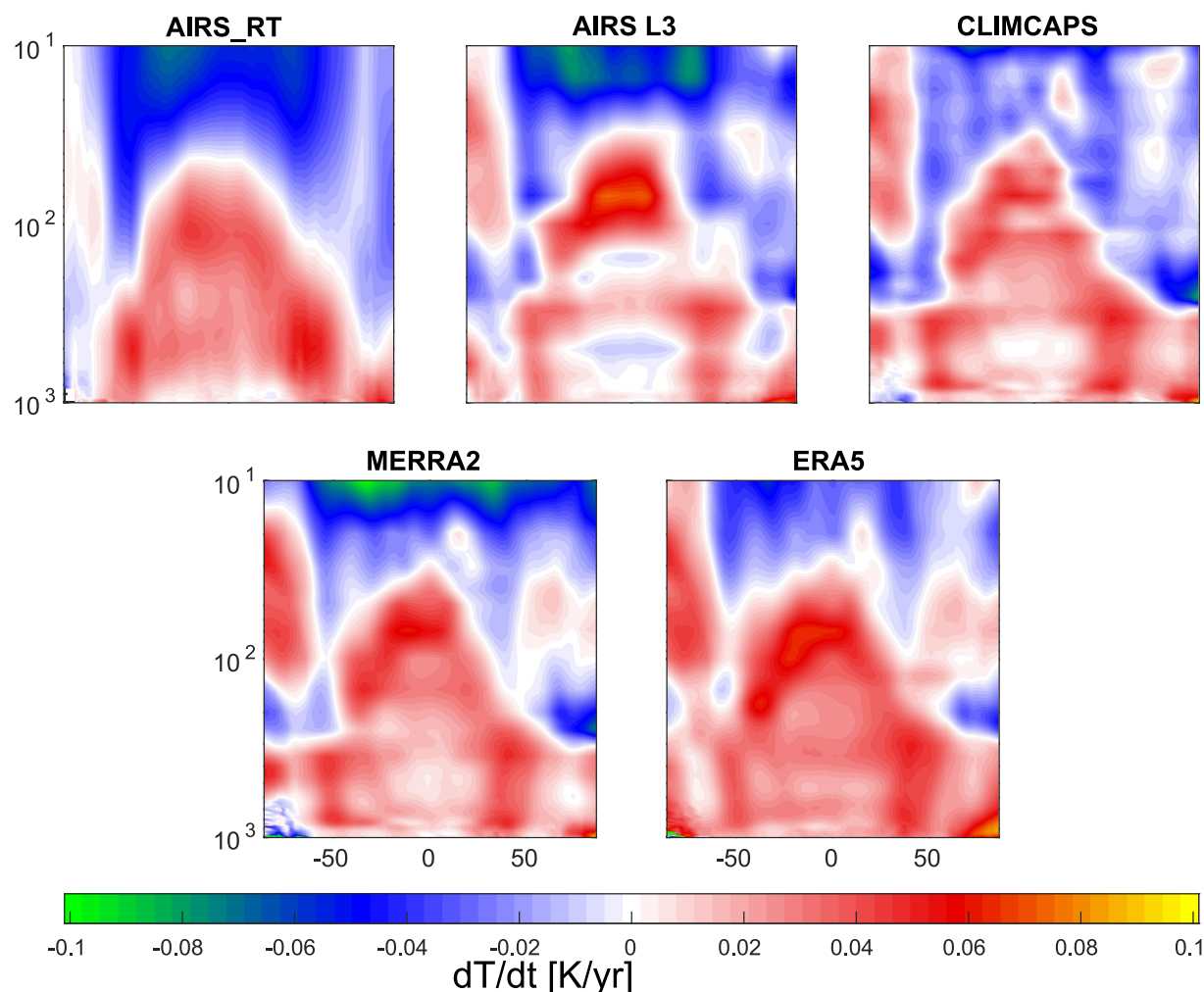


Figure 11. Zonally averaged dT/dt shown in 5 panels. The horizontal axis is in degrees latitude while the vertical axis is pressure (mb). The y-limits are between 10 and 1000 mb, on a logarithmic scale. The color bar is units of $K\ yr^{-1}$.

ERA5] fractional water vapor trends of Figure 12 (limited to 100 mb, 1000 mb) are [0.65,0.24,0.36,0.58], respectively.

Figure 13 shows the (smoothed) 400 mb fractional water vapor trends, with the left panel being the AIRS_RT trends while the right panel is the ERA5 trends. Note that there is general agreement except in the Southern Polar region, as also seen later in Figure 12 in the other two L3 retrieval data sets (AIRS v3 and CLIMCAPS). This could be related to work by Boisvert et al. (2019) who showed decreasing evaporation from the Southern Ocean in the 2003–2016 period due to increasing ice cover.

8. Uncertainty

The uncertainties for the AIRS v7 geophysical products are impacted by radiance noise amplification due to cloud clearing (Susskind et al., 2003) and the neural net first guess, while state vector errors are estimated based on regressions. CLIMCAPS L2 geophysical retrieval products are similarly impacted by cloud clearing noise in the radiances, but these are fully propagated together with geophysical error estimates from the MERRA2 first guess, through the retrieval algorithm which uses Optimal Estimation (Smith & Barnett, 2020). No estimate of uncertainties are available for the monthly L3 retrieved products.

The uncertainties for the retrieved AIRS_RT geophysical trends are straightforward to obtain using the OEM framework: the spectral uncertainties shown in Figure 5 are used together with the state vector covariance

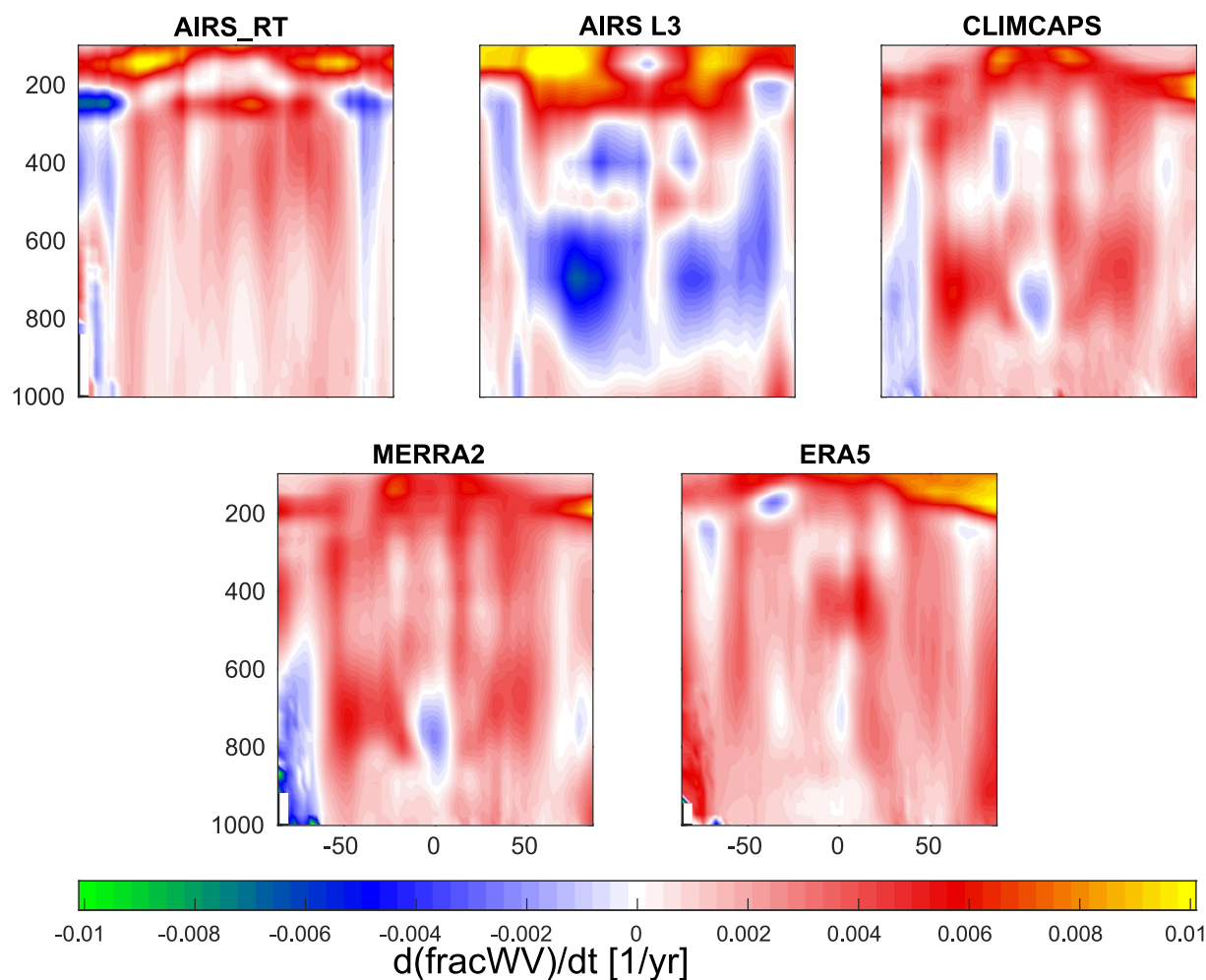


Figure 12. Zonally averaged dWV_{frac}/dt shown in 5 panels. Horizontal axis is latitude while vertical axis is pressure. The y-limits are between 100 and 1000 mb, on a linear scale. The color bar units are in yr^{-1} , as fractional water vapor is dimensionless.

matrices to generate the uncertainty matrix using the relevant equations from the OEM method; we use the diagonal elements for the final uncertainties. We refer the reader to Appendix A for a detailed discussion about the uncertainty in the radiance time series. Panels (A) and (C) of Figure 14 show the zonally averaged (D/N) uncertainties as a function of pressure and latitude. Inspection of the radiance trends uncertainties shown in the center panel of Figure 5 shows the upper atmosphere temperature sounding region ($650\text{--}700\text{ cm}^{-1}$) has much larger uncertainty in the polar regions. The instrument and spectroscopy characteristics, coupled with these observational uncertainties, are such that for temperature the smallest errors are in the tropics while the largest errors are in polar upper atmosphere, which are the regions below 100 mb where the ERA5 trends differ most from AIRS_RT trends. Similarly for water vapor the larger errors are in the lower atmosphere and above about 300 mb; the constant RH assumption and MLS *a priori* help alleviate the errors in the retrieved trends. We point out earlier work on studying upper tropospheric/lower stratospheric humidity over tropical cyclones also used MLS climatology together with AIRS observations (Feng & Huang, 2021).

The *Z-test* confirmed this picture, as seen in panels (B) and (D) of Figure 14, which show the temperature and fractional water vapor trends, together with black dots marking the (latitude, altitude) points where the trends are larger than the uncertainty in the trends, at the 5% significance level. This happens in panel (B) for the temperature trends in most of the tropical/mid-latitude free troposphere (and stratosphere) but not at the southern polar stratosphere; and in panel (D) for fractional water vapor trends in the 200–600 mb range, from the Southern Polar region to about +60° N latitude, and some spots in the Northern Polar.

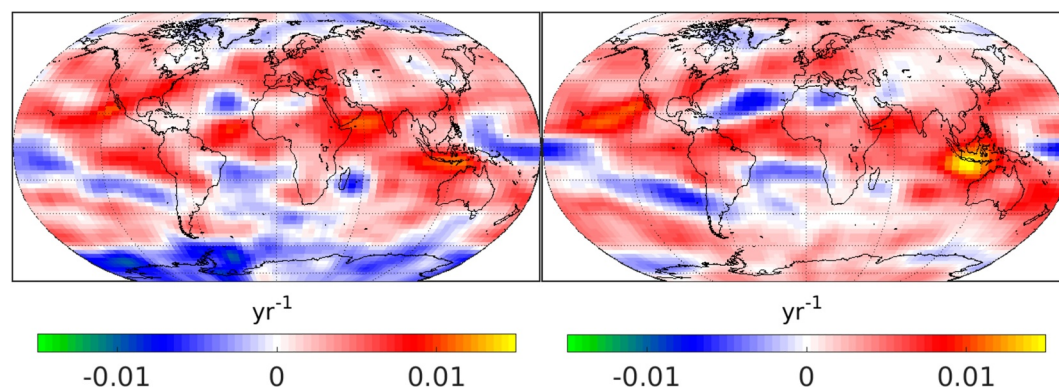


Figure 13. The 400 mb fractional water vapor trends for (left) AIRS_RT and (right) ERA5 show general agreement except in the Southern Polar Regions. The color bar units are in yr^{-1} , as fractional water vapor is dimensionless. Note these plots have been smoothed using a moving mean.

9. Discussion

In general for surface temperature trends, the disagreements between the six sets shown in Figure 7 are over the polar regions and over land (especially over the Amazon and Central Africa) and are smallest over tropical and mid-latitude oceans, indicating the best agreements, except for slightly larger differences off the western coast of the Americas and Africa (which have a prevalence of MBL clouds). The atmospheric temperature trends in general agreed except for the upper atmosphere polar regions and in the high altitudes (less than about 200 mb). Similarly fractional water vapor trends differed most in the upper atmosphere (200 mb and above) and in the tropical/mid-latitude 600–800 mb region. A quick glance at Figure 12 shows the former is due to lower sensitivity to upper atmosphere water vapor, leading the AIRS_RT retrievals to have low values while the AIRS L2 retrieval is initialized by a neural net; conversely the latter is due to the AIRS L3 retrieval being negative while the rest were mainly positive. Similarly the AIRS_RT retrieval differs above the Antarctic continent.

In general the observed surface temperature trends from the AIRS_RT retrievals agree with the ERA5 and MERRA2 trends, as well as the NASA GISS trends, except in the Southern Antarctic. That is a region where there are few surface observations; for retrievals there are competing effects of using ice versus ocean surface emissivity. Overall, the AIRS_RT retrieved surface temperature trends are typically in between ERA5 and MERRA2 for land + ocean in all regimes (tropical, midlatitude and polar), though slightly larger overall for ocean than the two reanalysis data sets; in general they are closer to the ERA5 trends than the MERRA2 trends.

(Strow et al., 2021) demonstrated that the long- and medium-wave channels of the AIRS instrument are radiometrically stable to better than $0.002\text{--}0.003 \text{ K yr}^{-1}$, which is much smaller than the surface and tropospheric temperature trends in the reanalysis models, AIRS L3 retrieved products and our retrieved trends. A separate analysis of spectral trend uncertainties after 05, 10, 15, 20 years (not shown here) show that these uncertainties have been steadily decreasing and are now approaching this number, as can be seen in the bottom left panel of Figure 3. Furthermore, though we cannot guarantee only cloud free scenes in our chosen Q0.90 observational data set used in this paper, the high correlations between other data set surface trends compared to ours, is a good indication that our results come from mostly cloud-free scenes, or scenes whose clouds have negligible impact on our results.

The observed zonal temperature trends agree with those from the models and the AIRS L3 operationally retrieved products, except in the polar regions. Again this could be an issue of using slightly incorrect surface emissivity for the AIRS_RT retrievals. In addition we point out that since there is very little water vapor, the temperature Jacobians near the surface are quite small in magnitude (compared to more humid atmospheres) and so it is difficult to separate out the effects of surface temperature trends versus lower atmosphere temperature and H_2O trends. The quantile construction used in this paper means that for example, tiles straddling the subcontinent of India and the ocean will preferentially pick the land surface observations for daytime, which could lead to misleading trends on these coastal tiles. It is possible to subdivide the $3^\circ \times 5^\circ$ tiles into for example, $1^\circ \times 1^\circ$ grids and do the analysis, but the number of observations per small grid cell would drop, leading to more noise in the retrieved trend.

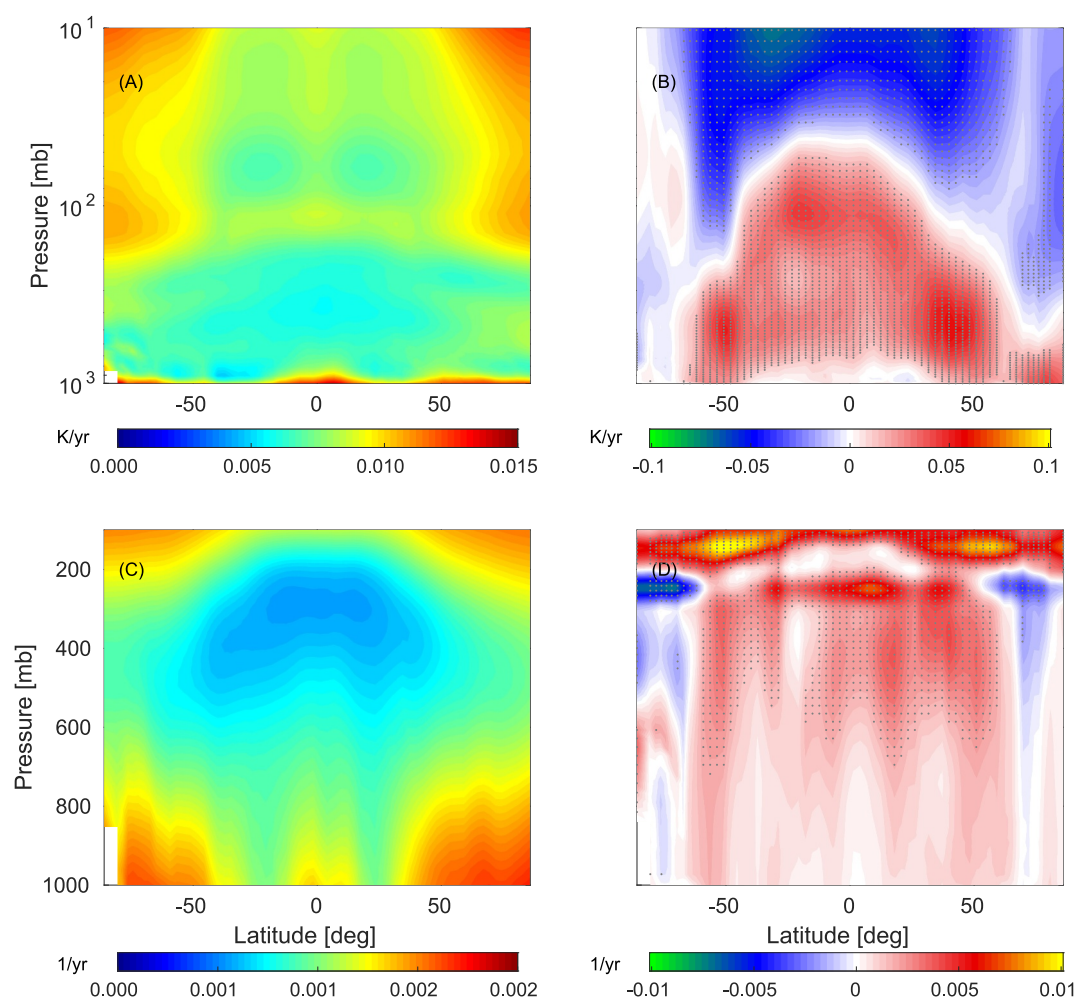


Figure 14. Zonally averaged D/N plots of (a) temperature uncertainties in K yr^{-1} and (b) temperature trends in K yr^{-1} . Panels (c) and (d) are the same except for fractional water vapor uncertainty and trends in yr^{-1} . The left hand panels are the geophysical uncertainties computed by the OEM retrieval, while the right hand panels show the retrieved trends together with black dots identifying where the Z-test indicates where the trends are larger than the uncertainty. Horizontal axes are in degrees latitude while vertical axis are pressure (mb)—logarithmic for temperature and linear for water vapor. See text for more detailed explanation.

In general the AIRS_RT retrieved column water trends are slightly smaller than ERA5 in the Southern Hemisphere but noticeably smaller in the Northern Tropics to midlatitudes. We have mentioned difficulties we have retrieving H_2O close to the surface and in the upper atmosphere, due to the known sensitivity of infrared sounders whose water vapor averaging kernels peak in the 300–600 mb range, even though examination of the spectral residuals in the window region shows we are fitting the signal. The MERRA2 and CLIMCAPS column water vapor trends are quite similar, while the AIRS v7 L3 retrieved trends are noticeably different, being negative almost everywhere. A zero *a priori* initialization for water vapor at the surface allows a fit to the spectral trends, but the retrieved water vapor trends in the lower layers which dominate column water amounts lead to column water trends that are easily double or more than the results for the other data sets. We have adjusted the OEM water vapor covariance matrices so that the zonally averaged column water trends agree in general with the other data sets.

Given the complex numerical algorithms used in both the reanalysis models and the AIRS L3 retrievals as well as those in the AIRS_RT trends, it is difficult to offer precise explanations for any of the trends shown above. Our results are relatively robust to changes in the covariance or Tikonov parameter settings. For instance changing them by factors of two would keep the trends about the same, though of course the uncertainties would change. There are however, a few general points that can be made. The first is that since infrared instruments are sensitive

to the 300–800 mb region and lose sensitivity outside this, the retrievals from AIRS_RT and AIRS L3 have difficulties with water vapor in the lower (Planetary Boundary Layer) and upper troposphere/lower stratosphere. One way to mitigate this is to use trended observed data from external sources in the *a priori*, while keeping the *a priori* trends for all other parameters as 0. For example, we have shown we can use the MLS observations above 300 mb without significantly degrading the AIRS_RT retrieval in the middle and lower atmosphere; conversely the CLIMCAPS retrievals are initialized by MERRA2 and while they can pull out weather signals, the trends from the L3 retrieved products are still quite closely tied to the MERRA2 trends. The tropical and mid-latitude ocean surface temperature trends from the numerical models that assimilate observed data, L3 retrieved products and AIRS_RT are very similar; however, they start to show differences where there are few *in situ* observations combined with problems with ice identification (surface emissivity)/cold temperatures which exacerbate the drifting AIRS detector problems (Strow et al., 2021), such as the Arctic and Southern Ocean.

10. Conclusions

We have designed a novel retrieval method, specifically to obtain global thermodynamic atmospheric climate trends. It uses long-term stable, high spectral resolution infrared all-sky hyperspectral observations which are the first subset for “nominally clear” scenes. The geophysical trends are derived using observed trends from the well-characterized (radiometrically stable) radiances and from zero *a priori* (except for a constant relative humidity assumption). This makes them much more direct and traceable than trends from traditional L2 retrieval algorithms, which use complicated *a priori* information. We also performed “radiative closure” tests by running the monthly reanalysis or L3 monthly retrieved data through a radiative transfer model to compare the spectral trends obtained against the observed spectral trends. The most noticeable disagreement in spectral trend radiance space was in the water vapor free troposphere sounding regions.

The temperature and water vapor trends retrieved from the “nominally clear” radiance trends resemble those computed from monthly ERA5 and MERRA2 reanalysis. The radiative spectral closure helps identify the cause of differences in the geophysical trends, rather than solely attributing them to deficiencies (e.g., the well-known reduced sensitivity to water vapor near the boundary layer and above 200 mb) with our retrieval. For example, the AIRS_RT temperature trends are quite similar to the reanalysis (MERRA2/ERA5) trends, while the water vapor (and/or Relative Humidity) trends are quite different, especially in the lower troposphere and upper troposphere, which is clearly manifest as differences in the spectral trends in the water vapor sounding region.

The 20 years of AIRS observations were binned into nominal 3×5 degree grid boxes covering the planet, with a time step of 16 days, from which anomalies and trends were obtained. To alleviate the reduced sensitivity of hyperspectral sounders to water vapor in the lower atmosphere we used an assumption of 0.01 increase in relative humidity to initialize the *a priori* lower atmosphere fractional water vapor rates, while we similarly used Microwave Limb Sounder trends as an *a priori* to address the high altitude water vapor deficiencies caused by lower sensitivity to upper atmosphere water vapor. Radiance trend error sources are discussed in detail in Appendix A, while differences in trends from reanalysis or L3 retrievals when the data are aggregated using the tile centers versus averaged over the tiles were discussed in Section 5. New or updated time dependent surface emissivity databases may become available in the future, enabling us to include those effects into Equation 4. Problems in the polar regions and Planetary Boundary Layer water vapor retrievals will be harder to overcome since there is very little sensitivity to water vapor in these regions, together with fewer observations to compare against, though more work is planned to address both of these.

In this paper we used the 90th quantile (Q0.90) nominally “hottest” observed BT1231 to form a time series over which to obtain radiance trends, after establishing that the spectral trends from this quantile differed by less than about $\pm 0.0015 \text{ K yr}^{-1}$ from the 50th (or average) quantile. In the future we plan to base the subset selection on MODIS cloud products (obtained at 1 km resolution compared to the AIRS 15 km resolution). In any case the AIRS L1C Q0.90 spectral trends used for the AIRS_RT results are very comparable to trends from quality assured binned AIRS CCR data (Manning, 2022). The quantile method allows us to select which observations to use in the trends: we have explored doing the trend retrievals using the cloud fields contained in ERA5, together with the TwoSlab cloud algorithm (De Souza-Machado et al., 2018) to compute Jacobians when clouds are present, together with trends from the Q0.50 observational data set described above. The retrieved geophysical trends resemble those described above in the mid to upper atmosphere, and differ in the lower atmosphere, but more work is needed and is not discussed further. Zonally averaged longwave clear sky flux trends (both outgoing top-

of-atmosphere and incoming bottom-of-atmosphere) derived using sums over the flux changes arising from the AIRS_RT surface temperature, and atmospheric water vapor, ozone and temperature trends together with flux changes induced by CO₂,CH₄ forcings in general agree with those derived using observational flux trends from the Cloud and Earth's Radiant Energy (CERES) clear sky Energy Balanced and Filled (EBAF) Level 3b product (Kato et al., 2018; Loeb et al., 2018).

While the Aqua platform is scheduled to be terminated within the next few years, copies of nearly identical CrIS instruments are already in orbit, and more will be launched over the next few years, till at least 2040. The Climate Hyperspectral Infrared Radiance Product (CHIRP) (Strow et al., 2021) will seamlessly combine the AIRS observations between 2002 and 2015 to CrIS observations from 2015 to 2040 to obtain a 40 year observational radiance record over which to study climate. This availability means that the current AIRS_RT and future AIRS/CrIS radiance version, is well-positioned to enable climate analysis of geophysical trends and anomalies for years to come.

Appendix A: Summary of Noise and Uncertainty in Radiance Time Series

The uncertainties in the geophysical 20-year linear trends reported depend upon the uncertainties in the 20-year radiance trends directly derived from the AIRS radiance observations. The radiance trend uncertainties are the standard errors of the linear term, a_1 in Equation 2. Note that the standard deviation is taken over the 460 16-day bins that make up our radiance time series. In ideal conditions the time series of fit residuals of Equation 2 would be the AIRS detector noise. However, the observed fit residuals are almost always dominated by other processes. This would be true of any climate signal that is subject to variability induced by weather and inter-annual variability, which often requires multi-decade records to recover accurate trends.

Various contributors to the radiance trend uncertainties include: (a) detector noise, (b) radiance anomalies that are not linear in time (inter-annual variability, greenhouse growth rates, etc), (c) sampling noise that includes temporal and spatial variability within our nominal 3×5 latitude/longitude 16-day sampling grid, (d) similar variability among the 16-day sampling time-steps, and (e) variability in the satellite zenith viewing angle among the different 16-day sampling steps. The origin of the noise/variability in these time series does not directly affect the results of this work, other than possibly as a guide for finding better sampling approaches for future work. Here we give a brief outline of the size of the fit residual standard deviations and a more detailed look at the origin of the variability of the residuals for two different channels for two tiles.

Detector noise is inconsequential in this work since each 16-day mean radiance is an average over ~ 500 observations per spectral channel. This reduces the standard error in the mean by a factor of $\sim 22 (\sqrt{500})$. Comparisons of the detector noise to the observed variability in the radiance time series fit residuals show that detector noise is $\sim 25X$ to $150X$ smaller than the observed variability.

The dominant sources of variability arise from items (b)–(e) listed above. Examination of the global maps of the radiance trend fit residuals for four channels largely provides insights into the spatial variability in these uncertainties. These channels are the 670 cm^{−1} stratospheric CO₂ channel, the 732 cm^{−1} tropospheric CO₂, the 1231 cm^{−1} surface temperature channels, and the water vapor channel at 1500 cm^{−1}. Table A1 lists the global range of fit residual standard deviations for these channels. Often they are in the 1–2K range with higher variability often seen in polar regions. The variability in the water vapor channel is different in that it is largest in the tropics where

spatial and temporal variability can be quite large. Overall the lowest variability in the 1231 cm^{−1} surface channel, and the highest variability in the polar stratospheric channel at 670 cm^{−1}. We examine them in more detail below.

ENSO related inter-annual variability (anomalies) cannot be completely modeled with a simple linear trend. However, any inter-annual anomalies can be examined in our data set by smoothing over the more random sampling noise in the fit residuals of time-series regression. Figure A1 shows a smoothed version of the 1231 cm^{−1} channel fit residual for a tile in the tropical Eastern Pacific (1.37° S, 137.5° W). The residual (red curve) has been smoothed with loess filter (quadratic) 1-year in length. Also plotted is the

Table A1
Fit Residual Standard Deviations for Several Representative AIRS Channels

Channel cm ^{−1}	Residual std in K
670	1–2 K, but up to 5 + K in polar regions
710	0.5–1.9 K
732	0.5–3 K
1231	0.37–5 K
1500	1.4–4.5 K (high in tropics)

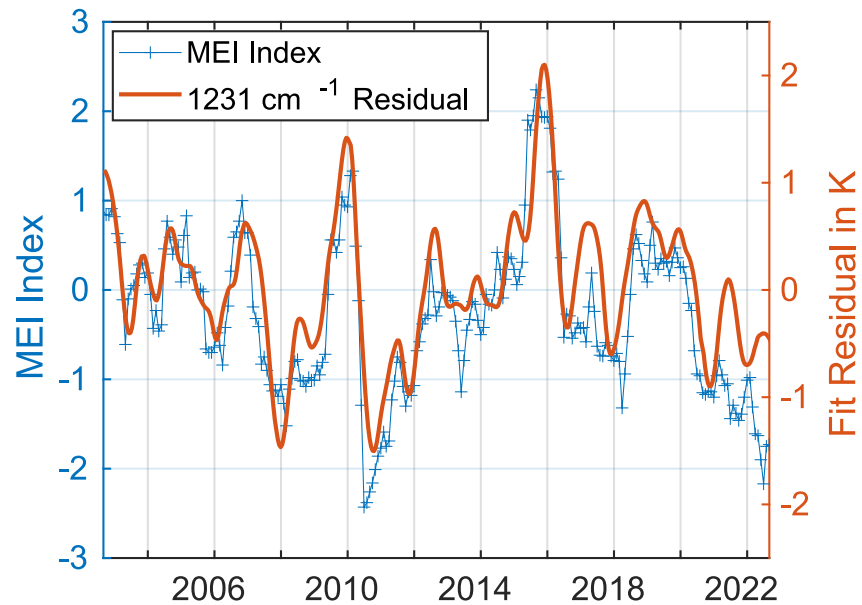


Figure A1. MEIV2 index compared to 1231 cm^{-1} fit residual for tiled grid bin at 1.37°S , 137°W .

NOAA MEIV2 ENSO index (NOAA Physical Sciences Laboratory, 2011) for the same time period. Clearly, the smoothed residual for this single tile closely follows the overall MEIV2 index. Note that the more smooth ENSO anomalies are partially accounted for in our trend uncertainties by including the lag-1 autocorrelation correction (see Section 3.2).

The raw residual standard deviation for this tile is 0.72K RMS , while the standard deviation of the smoothed residual shown in Figure A1 is 0.65K RMS . Using the sum of squares for Gaussian noise, this gives a value of 0.31K RMS for the more rapid variations in the residual. We have simulated the effect of the variation in satellite

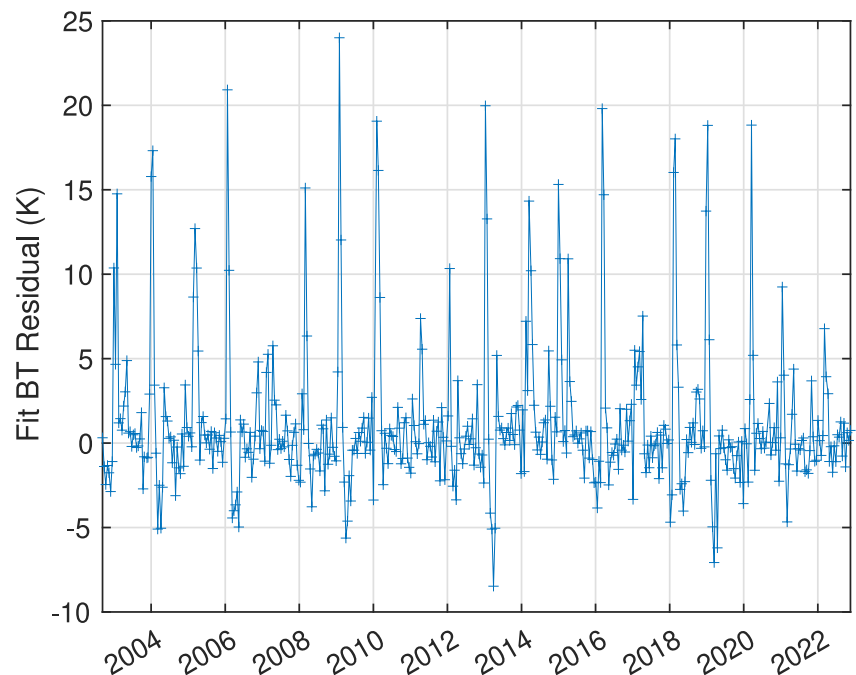


Figure A2. Trend fit residuals for the 670 cm^{-1} channel tile centered at 59°N , -102°W , which clearly exhibit sudden stratospheric warmings in the winter months.

zenith angle for this channel and tile, which is only 0.04K RMS. Therefore in this particular example the ENSO variations dominate the noise although the fast random sampling terms are far from zero.

The contribution of slightly varying satellite viewing zenith angles will be a maximum in the CO₂ long-wave sounding region, centered near the 730 cm⁻¹ channel. A similar analysis of the noise components of the fit residual for this channel gives a raw residual standard deviation of 0.61K RMS, while the standard deviation of the smoothed residual is 0.40 K RMS. (Some ENSO variability is seen in this channel.) Using the sum of squares for noise, this gives a value of 0.47 K RMS for the more rapid variations in the residual. The simulated effect of the variation in satellite zenith angle is 0.27 K RMS. Again, using the sum of the squares of the RMS values for the satellite zenith variations we obtain a value of 0.38 K RMS for the variations in the rapidly changing part of the residual. This suggests that a small component of the residual is due to the slight variations in the satellite zenith viewing angle, it is far from dominant and that the ENSO variations and the fast random sampling terms dominate the observation noise. In general the satellite secant angles, although variable from tile to tile, did not exhibit any drifts that would impact the trend results shown here.

The stratospheric channels often exhibit very high fit residual standard deviations in the North Polar regions. Figure A2 shows the 670 cm⁻¹ channel fit residuals for a tile centered at 59°N, -102°W (slightly west of the Hudson Bay in Canada). Extremely large spikes are seen in the winter months caused by sudden stratospheric warming (SSW) (Butler et al., 2015). These spikes are far above the background noise in the residuals since they can be as large as 10–25K. These SSW spikes increase the fit residual standard deviation by more than a factor of two. In this work no attempt was made to filter the SSWs from the radiance time series.

Appendix B: Day Versus Night Surface Temperature Trend Differences

Figure B1 shows the (top) daytime and (middle) nighttime surface temperature trends; from left to right the data sets are (observational) AIRS_RT, (operational retrievals) AIRS L3, CLIMCAPS L3, and (reanalysis) ERA5. In general the AIRS observations show enhanced daytime cooling over the Indian subcontinent and Central Africa, compared to the ERA5 model; they also show daytime warming trends over continental Europe and central Asia and the Amazon are larger than during the nighttime. With the large ocean heat capacity and smaller land heat capacity, the land is expected to show more of a diurnal cycle than ocean. ERA5 sees warming over Eastern/Central Africa during daytime while the observations show cooling. Similarly the three observations show more daytime cooling over the Indian sub-continent and south eastern Australia than does ERA5; we omit more detailed analysis in this paper. During the nighttime, the AIRS v7 L3 operational retrieval has cooling over C. Africa and parts of the Amazon. The day–night differences are seen in the bottom row of the same figure. Note the color bar is the same for all three rows. The differences are close to zero over the ocean. AIRS_RT and CLIMCAPS L3 retrievals see more daytime cooling over E. Africa and the Indian subcontinent. Overall the magnitude of the day–night differences for the observations are larger for the AIRS observations than for ERA5. ERA5 also sees negative differences over Central Asia compared to the AIRS observations, which see positive differences (higher surface temperature trends during the daytime).

The atmospheric temperature and fractional water vapor day–night differences are quite small (compared to the average values) and not shown here; AIRS v7 L3 operational retrievals show noticeable more wetting of the 600–800 mb region during daytime versus nighttime, compared to the other three.

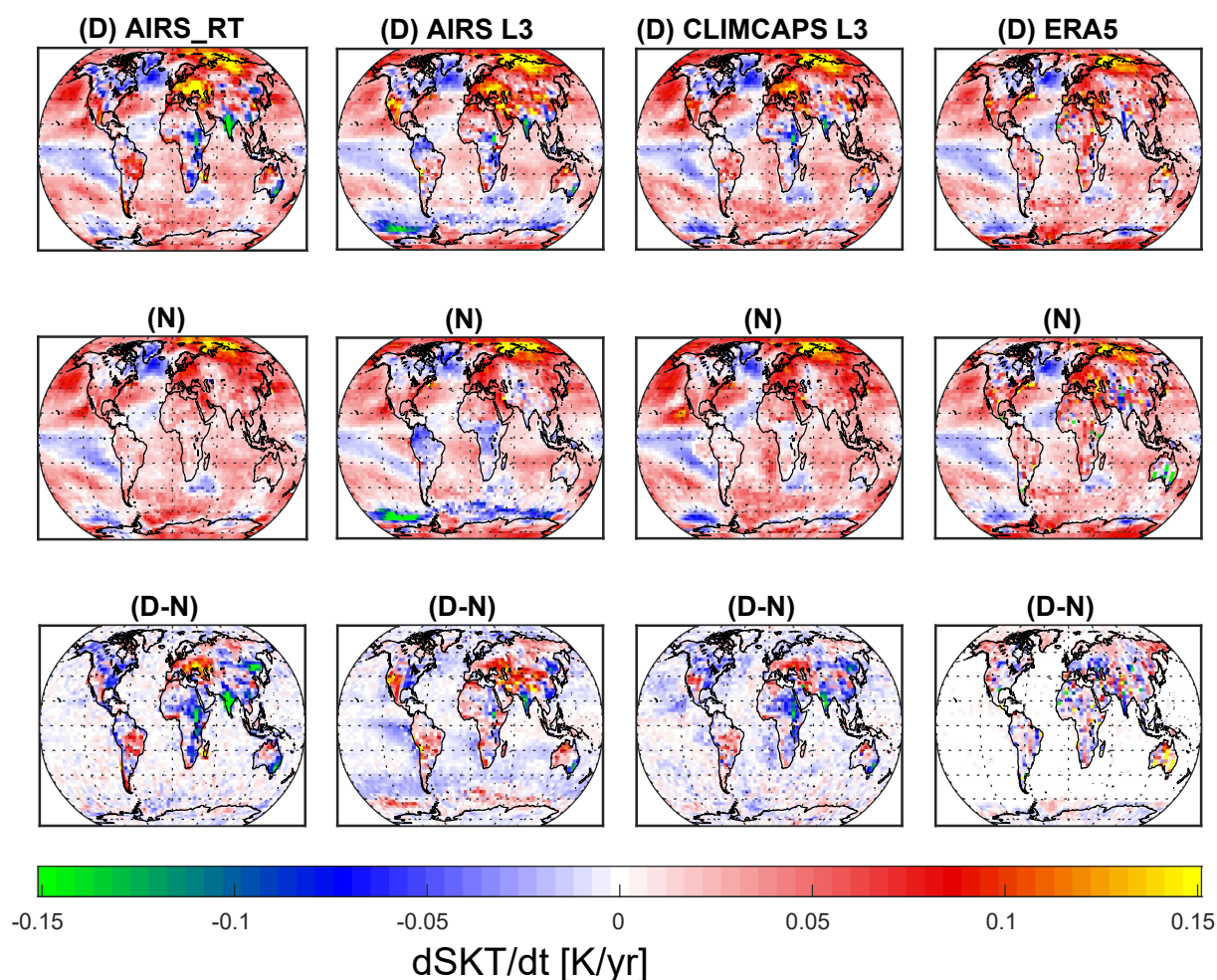


Figure B1. Top two rows: The (top) day and (middle) night surface temperature trends for AIRS_RT, AIRS L3, CLIMCAPS L3 and ERA5. Third row (bottom) is the D-N difference. Color bar units are in $K\ yr^{-1}$.

Conflict of Interest

The authors declare no conflicts of interest relevant to this study.

Data Availability Statement

The observations used in this paper (AIRS L1C radiances), as well as the (AIRS L3, CLIMCAPS L3, MLS L3) monthly retrievals, and MERRA-2 monthly geophysical fields, are freely available to the public on the NASA Goddard Space Flight Center Earth Sciences (GES) Data and Information Services Center (DISC) servers <https://disc.gsfc.nasa.gov/>. Monthly ERA5 model output at both single level (scalar) and pressure levels (vector) is freely available through Hersbach et al. (2023). GISTEMP monthly model outputs are also freely available from <https://data.giss.nasa.gov/gistemp/>. The F90 kCARTA (De Souza-Machado et al., 2018) line-by-line code used to make the Jacobians is freely available on https://github.com/sergio66/kcarta_gen (DeSouza-Machado, 2025a). Questions about obtaining the kCARTA database can be directed to Sergio DeSouza-Machado (sergio@umbc.edu). The Matlab source code and .mat files used to make the plots, and the climate analysis code, are available on https://github.com/sergio66/JGR_July2025.git (DeSouza-Machado, 2025b). Questions about the matlab based source code used for the analysis can be directed to Sergio DeSouza-Machado (sergio@umbc.edu).

Acknowledgments

We gratefully acknowledge the help of H. Motteler, who designed, implemented and ran the AIRS tiling code. C. Hepplewhite helped test the outputs of the tiling code. S. Buczkowski worked on bringing down almost all the data used in this study, and made the uniform/clear observational data sets. Chris Barnett has given helpful comments and general advice regarding retrievals and comparisons to the AIRSv7 and CLIMCAPS data sets. Jing Feng provided valuable feedback regarding the manuscript. The authors would also like to thank the two anonymous referees for their valuable comments that substantially improved the manuscript. This work was performed under NASA Grant 80NSSC22K0702. The hardware used is part of the UMBC High Performance Computing Facility (HPCF). The facility is supported by the U.S. National Science Foundation through the MRI program (Grants CNS-0821258, CNS-1228778, OAC-1726023, and CNS-1920079) and the SCREMS program (Grant DMS-0821311), with additional substantial support from the University of Maryland, Baltimore County (UMBC). See hpcf.umbc.edu for more information on HPCF and the projects using its resources.

References

- AIRS Project Office. (2015). Atmospheric infrared sounder level 1C algorithm theoretical basis document. (Tech. Rep.). Retrieved from https://eosps.nasa.gov/sites/default/files/atbd/V6.1.0_201_AIRS_L1C_ATBD.pdf:EOS-GSFC
- Allan, R., Willett, K. M., John, V., & Trent, T. (2022). Global changes in water vapor 1979–2020. *Journal of Geophysical Research*, 127(12), e2022JD036728. <https://doi.org/10.1029/2022JD036728>
- Andersson, E., Holm, E., Bauer, P., Bejaars, A., Kelly, G., McNally, A., et al. (2007). Analysis and forecast impact of the main humidity observing systems. *Quarterly Journal of the Royal Meteorological Society*, 133(627), 1473–1485. <https://doi.org/10.1002/qj.112>
- Boisvert, L., Vihma, T., & Shie, C.-L. (2019). Evaporation from the southern ocean estimated on the basis of AIRS satellite data. *Journal of Geophysical Research*, 125(1). <https://doi.org/10.1029/2019JD030845>
- Borbas, E., Hulley, G., Feltz, M., Knuteson, R., & Hook, S. (2018). The combined ASTER MODIS emissivity over land (CAMEL) Part 1: Methodology and high spectral resolution application. *Remote Sensing*, 10(4), 643. <https://doi.org/10.3390/rs10040643>
- Borger, C., Beirle, S., & Wagner, T. (2022). Analysis of global trends of total column water vapour from multiple years of OMI observations. *Atmospheric Chemistry and Physics*, 22(16), 10603–10621. <https://doi.org/10.5194/acp-22-10603-2022>
- Brindley, H., Bantges, R., Russell, J., Murray, J., Dancel, C., Belotti, C., & Harries, J. (2015). The spectral signature of Earth's climate variability over 5 years from IASI. *Journal of Climate*, 28, 1649–1660. <https://doi.org/10.1175/JCLI-D-14-00431.1>
- Bromwich, D., Ensign, A., Wang, S.-H., & Zou, X. (2024). Major artifacts in ERA5 2-m air temperature trends over Antarctica prior to and during the modern satellite era. *Geophysical Research Letters*, 51(21). <https://doi.org/10.1029/2024GL111907>
- Butler, A., Seidel, D., Hardiman, S., Butchart, N., Birner, T., & Match, A. (2015). Defining sudden stratospheric warming. *BAMS*, 96(11), 1913–1928. <https://doi.org/10.1175/BAMS-D-13-00173.1>
- Cai, M., & Kalnay, E. (2004). Can reanalysis have anthropogenic climate trends without model forcing? *Journal of Climate*, 18(11), 1844–1849. <https://doi.org/10.1175/jcli3347.1>
- Carn, S., Strow, L., DeSouza-Machado, S., Edmonds, Y., & Hannon, S. (2005). Quantifying tropospheric volcanic eruptions with AIRS: The 2002 eruption of Mt. Etna (Italy). *Geophysical Research Letters*, 32(2), L02301. <https://doi.org/10.1029/2004GL021034>
- Chedin, A., Barnett, C., Olsen, E., Chen, L., & Maddy, E. (2005). On the determination of atmospheric minor gases by the method of vanishing partial derivatives with application to CO₂. *Geophysical Research Letters*, 32(22), L22803. <https://doi.org/10.1029/2005GL024165>
- Chung, E., Soden, B., Sohn, B., & Shi, L. (2014). Upper-tropospheric moistening in response to anthropogenic warming. *PNAS*, 111(32), 11636–11641. <https://doi.org/10.1073/pnas.1409659111>
- Clough, S., Shephard, M., Mlawer, E., Delamere, J., Iacono, M. J., Cady-Pereira, K., et al. (2005). Atmospheric radiative transfer modeling: A summary of the AER codes. *Journal of Quantitative Spectroscopy and Radiative Transfer*, 91(2), 233–244doi. <https://doi.org/10.1016/j.jqsrt.2004.05.058>
- Dee, D., Kallen, E., Simmons, A., & Haimberger, L. (2011). Comments on reanalyses suitable for characterizing long-term trends. *BAMS*. <https://doi.org/10.1175/2010BAMS3070.1>
- DeSouza-Machado, S. (2025a). *KCARTA F90 code V1.22R1*. Zenodo. <https://doi.org/10.5281/zenodo.15785097>
- DeSouza-Machado, S. (2025b). *Matlab plotting code and climate analysis source code for JGR 2025 paper, V1.03*. Zenodo. <https://doi.org/10.5281/zenodo.15817128>
- De Souza-Machado, S., Strow, L. L., Imbira, B., McCann, K., Hoff, R., Hannon, S., et al. (2010). Infrared retrievals of dust using AIRS: Comparisons of optical depths and heights derived for a North African dust storm to other collocated EOS A-Train and surface observations. *Journal of Geophysical Research*, 115(D15), D15201. <https://doi.org/10.1029/2009JD012842>
- De Souza-Machado, S., Strow, L. L., Motteler, H., & Hannon, S. (2020). kCARTA: A fast pseudo line by line radiative transfer algorithm with analytic Jacobians, fluxes, non-local thermodynamic equilibrium and scattering. *Atmospheric Measurement Techniques*, 31, 323–339. <https://doi.org/10.5194/amt-13-323-2020>
- De Souza-Machado, S., Strow, L. L., Tangborn, A., Huang, X., Chen, X., Liu, X., et al. (2018). Single-footprint retrievals for AIRS using a fast TwoSlab cloud-representation model and the SARTA all-sky infrared radiative transfer algorithm. *Atmospheric Measurement Techniques*, 11(1), 529–550. <https://doi.org/10.5194/amt-11-529-2018>
- Feng, J., & Huang, Y. (2021). Impacts of tropical cyclones on the thermodynamic conditions in the tropical tropopause layer observed by A-Train satellites. *Advanced Manufacturing Technology*, 21(2-), 15493–15518. <https://doi.org/10.5194/amt-21-15493-2021>
- Friedlingstein, P., Jones, M. W., O'Sullivan, M., Andrew, R. M., Bakker, D. C. E., Hauck, J., et al. (2022). Global carbon budget 2021. *Earth System Science Data*, 14(4), 1917–2005. <https://doi.org/10.5194/essd-14-1917-2022>
- Fu, D., Kulawik, S., Bowman, J., Worden, K., & Eldering, A. (2018). Retrievals of tropospheric ozone profiles from the synergism of AIRS and OM methodology and validation. *Advanced Manufacturing Technology*, 11, 5587–5605. <https://doi.org/10.5194/amt-11-5587-2018>
- Gelaro, R., McCarty, W., Suárez, M. J., Todling, R., Molod, A., Takacs, L., et al. (2017). MERRA-2 overview: The modern-era retrospective analysis for research and applications, version 2 (MERRA-2). *Journal of Climate*, 30, 5419–5454. <https://doi.org/10.1175/JCLI-D-16-0758.1>
- GISTEMP Team. (2025). GISS surface temperature analysis (GISTEMP), version 4. (Tech. Rep.). Retrieved from <https://data.giss.nasa.gov/gistemp/>:NASA/GoddardInstituteforSpaceStudies
- Gordon, I., Rothman, L. E. A., Hargreaves, R., Hashemi, R., Karlovets, E., Skinner, F., et al. (2022). The HITRAN 2020 molecular spectroscopic database. *Journal of Quantitative Spectroscopy and Radiative Transfer*, 277, 1–82. <https://doi.org/10.1016/j.jqsrt.2021.107949>
- Haiden, T., Dahoui, M., Ingleby, B., de Rosnay, P., Prates, C., Kuscus, E., et al. (2018). Use of in situ surface observations at ECMWF (No. 834). Harries, J., Brindley, H., & Geer, A. (1998). Climate variability and trends from operational satellite spectral data. *Geophysical Research Letters*, 25(21), 3975–3978. <https://doi.org/10.1029/1998GL000056>
- He, H., Kramer, R., & Soden, B. (2021). Evaluating observational constraints on intermodel spread in cloud, temperature and humidity feedbacks. *Geophysical Research Letters*, 48(17). <https://doi.org/10.1029/2020gl092309>
- Held, I., & Soden, B. (2000). Water vapor feedback and global warming. *Annual Review of Energy and the Environment*, 25(1), 441–475. <https://doi.org/10.1146/annurev.energy.25.1.441>
- Hersbach, H., Bell, B., Berrisford, P., Biavati, G., Horányi, A., Muñoz Sabater, J., et al. (2023). ERA5 monthly averaged data on single levels from 1940 to present. *Copernicus Climate Change Service (C3S) Climate Data Store (CDS)*. <https://doi.org/10.24381/cds.f17050d7>
- Hersbach, H., Bell, B., Berrisford, P., Hirahara, S., Horányi, A., Muñoz-Sabater, J., et al. (2020). The ERA5 global reanalysis. *Quarterly Journal of the Royal Meteorological Society*, 146(730), 1999–2049. <https://doi.org/10.1002/qj.3803>
- Hobbs, W., Klekociuk, A., & Pan, Y. (2020). Validation of reanalysis Southern Ocean atmosphere trends using sea ice data. *Atmospheric Chemistry and Physics*, 20(23), 14757–14768. <https://doi.org/10.5194/acp-20-14757-2020>
- Houghton, J., Jenkins, G. J., & Ephraums, J. J. (1990). *Climate change, the IPCC scientific assessment*. Cambridge University Press.

- Huang, X., Chen, X., Fan, X., Kato, S., Loeb, N., Bosilovich, M., et al. (2023). A synopsis of AIRS global-mean clear-sky radiance trends from 2003 to 2020. *Journal of Geophysical Research*, 127(24), e2022JD037598. <https://doi.org/10.1029/2022JD037598>
- Huang, Y., Ramaswamy, V., Huang, X., Fu, A., & Bardeen, C. (2007). A strict test in climate modeling with spectrally resolved radiances: GCM simulation versus AIRS observations. *Geophysical Research Letters*, 34(24), L24707. <https://doi.org/10.1029/2007GL031409>
- IPCC. (2021). *Climate change 2021 - The physical science basis*. Cambridge University Press. <https://doi.org/10.1017/9781009157896>
- Irion, F., Kahn, B., Schreier, M., Fetzer, E., Fishbein, E., Fu, D., et al. (2018). Single-footprint retrievals of temperature, water vapor and cloud properties from AIRS. *Atmospheric Measurement Techniques*, 11(2), 971–995. <https://doi.org/10.5194/amt-11-971-2018>
- Kahn, B., Eldering, A., Fetzer, E., Fishbein, E., Lee, S.-Y., Liou, K., et al. (2005). Nighttime cirrus detection using the atmospheric infrared sounder window channels and total column water vapor. *Journal of Geophysical Research*, 110(D7), D07203. <https://doi.org/10.1029/2004JD005430>
- Kahn, B., Irion, F., Dang, V., Manning, E., Nasiri, S., Naud, C., et al. (2014). The atmospheric infrared sounder version 6 cloud products. *Atmospheric Chemistry and Physics*, 14(1), 399–426. <https://doi.org/10.5194/acp-14-399-2014>
- Kalnay, E., Kanamitsu, M., Kistler, R., Collins, W., Deaven, D., Gandin, L., et al. (1996). The NCEP/NCAR 40-year reanalysis project. *Bulletin of the American Meteorological Society*, 77(D20S93), 437–472. [https://doi.org/10.1175/1520-0477\(1996\)077<0437:TNYRP>2.0.CO;2](https://doi.org/10.1175/1520-0477(1996)077<0437:TNYRP>2.0.CO;2)
- Kato, S., Rose, F., Rutan, D., Thorsen, T., Loeb, N. G., Doelling, D., et al. (2018). Surface irradiances of edition 4.0 clouds and the Earth's radiant energy system (CERES) energy balanced and filled (EBAF) data product. *Journal of Climate*, 31(11), 4501–4527. <https://doi.org/10.1175/JCLI-D-17-0523.1>
- Keeling, C., Bacastow, R., Bainbridge, A., Ekdahl, C., Guenther, P., Waterman, L., & Chin, J. F. S. (1976). Atmospheric carbon dioxide variations at Mauna Loa observatory, Hawaii. *Tellus*, 28(6), 538–551. <https://doi.org/10.1111/j.2153-3490.1976.tb00701.x>
- King, M., Platnick, S., Menzel, P., Ackerman, S., & Hubanks, P. (2013). Spatial and temporal distribution of clouds observed by MODIS onboard the terra and aqua satellite. *IEEE*, 51(7), 3826–3852. <https://doi.org/10.1109/TGRS.2012.2227333>
- KISS Continuity Study Team. (2024). Toward a US framework for continuity of satellite observations of Earth's climate and for supporting societal resilience. *Earth's Future*, 12(2). <https://doi.org/10.1029/2023ef003757>
- Kistler, C., Kalnay, E., Collins, W., Saha, S., White, G., Woollen, J., et al. (2001). The NCEP-NCAR 50-year reanalysis: Monthly means CD-ROM and documentation. *BAMS*, 82(2), 247–267. [https://doi.org/10.1175/1520-0477\(2001\)082<0247:tnnym>2.3.co;2](https://doi.org/10.1175/1520-0477(2001)082<0247:tnnym>2.3.co;2)
- Kramer, R. J., He, H., Soden, B. J., Oreopoulos, L., Myhre, G. F., Forster, P. M., & Smith, C. (2021). Observational evidence of increasing global radiative forcing. *Geophysical Research Letters*, 48(7). <https://doi.org/10.1029/2020gl091585>
- Lambert, A., Read, W., Livesey, N., & Fuller, R. (2021). MLS/aura level 3 monthly binned vapor (H₂O) mixing ratio on assorted grids V005. (Tech. Rep.). Retrieved from [https://disc.gsfc.nasa.gov/datasets/ML3MBH2O_005/summary?NASAGreenbelt,MD,USA,GoddardEarthSciencesDataandInformationServicesCenter\(GESDISC\)](https://disc.gsfc.nasa.gov/datasets/ML3MBH2O_005/summary?NASAGreenbelt,MD,USA,GoddardEarthSciencesDataandInformationServicesCenter(GESDISC))
- Lambert, A., Read, W., Livesey, N., Santee, M., Manney, G., Froidevaux, L., et al. (2007). Validation of the aura microwave limb sounder middle atmosphere water vapor and nitrous oxide measurements. *Journal of Geophysical Research*, 112(D24). <https://doi.org/10.1029/2007JD008724>
- LeMarshall, J., Jung, J., Deber, J., Chahine, M. R. T., Lord, S., et al. (2006). Improving global analysis and forecasting with AIRS. *Bulletin of the American Meteorological Society*, 87, 891–894. <https://doi.org/10.1175/BAMS-87-7-891>
- Lenssen, N., Schmidt, G., Hansen, J., Menne, M., Persin, A., Ruedy, R., & Zyss, D. (2019). Improvements in the GISTEMP uncertainty model. *Journal of Geophysical Research*, 124(12), 6307–6326. <https://doi.org/10.1029/2018JD029522>
- Lenssen, N., Schmidt, G., Hendricksen, M., Jacobs, P., Menne, M., & Ruedy, R. (2024). A GISTEMPv4 observational uncertainty ensemble. *Journal of Geophysical Research*, 129(17), e2023JD040179. <https://doi.org/10.1029/2023JD040179>
- Lin, Y., & Oey, L. (2020). Global trends of sea surface gravity wave, wind, and coastal wave setup. *Journal of Climate*, 33(3), 769–785. <https://doi.org/10.1175/JCLI-D-19-0347.1>
- Livesey, N., Van Snder, W., Read, W., & Wagner, P. (2006). Retrieval algorithms for the EOS microwave limb sounder (MLS). *IEEE*, 44, 1144–1155.
- Loeb, N. G., Doelling, D., Wang, H., Su, W. C. N., Corbett, J., Kato, S., et al. (2018). Clouds and the Earth's radiant energy system (CERES) energy balanced and filled (EBAF) top-of-atmosphere (TOA) edition-4.0 data product. *Journal of Climate*, 31(2), 895–918. <https://doi.org/10.1175/JCLI-D-17-0208.1>
- Loeb, N. G., Johnson, G. C., Thorsen, T. J., Lyman, J. M., Rose, F. G., & Kato, S. (2021). Satellite and ocean data reveal marked increase in Earth's heating rate. *Geophysical Research Letters*, 48(13). <https://doi.org/10.1029/2021gl093047>
- Maddy, E., & Barnet, C. (2008). Vertical resolution estimates in version 5 of AIRS operational retrievals. *IEEE*, 66(8), 2375–2384. <https://doi.org/10.1109/TGRS.2008.917498>
- Manabe, S., & Wetherald, R. T. (1967). Thermal equilibrium of the atmosphere with a given distribution of relative humidity. *Journal of the Atmospheric Sciences*, 24(3), 241–259. [https://doi.org/10.1175/1520-0469\(1967\)024<0241:teotaw>2.0.co;2](https://doi.org/10.1175/1520-0469(1967)024<0241:teotaw>2.0.co;2)
- Manning, E. (2022). NASA JPL private communication, 4/2022. (AIRS CCR L3 data).
- Manning, E., Aumann, H., Broberg, S., Pagano, T., Wilosn, R., Yanovsky, I., & Strow, L. (2020). *EOS AIRS LIC data product user guide*. (Tech. Rep.). NASA. Retrieved from https://docserv.gesdisc.eosdis.nasa.gov/public/project/AIRS/V6.7_LIC_Product_User_Guide.pdf
- Masuda, K., Takashima, T., & Takayama, Y. (1988). Emissivity of pure and sea waters for the model sea surface in the infrared window regions. *Remote Sensing of Environment*, 24(2), 313–329. [https://doi.org/10.1016/0034-4257\(88\)90032-6](https://doi.org/10.1016/0034-4257(88)90032-6)
- McMillan, W., Barnet, C., Strow, L., Chahine, M., MCCourt, M., Warner, J., et al. (2005). Daily global maps of carbon monoxide from NASA's atmospheric airs sounder. *Geophysical Research Letters*, 32(11), L11801. <https://doi.org/10.1029/2004gl021821>
- Mears, C., & Wentz, F. (2009). Construction of the remote sensing systems v3.2 atmospheric temperature records from the MSU and AMSU microwave sounders. *Journal of Atmospheric and Oceanic Technology*, 26(6), 1040–1056. <https://doi.org/10.1175/2008JTECHA1176.1>
- Mears, C., & Wentz, F. (2016). Sensitivity of satellite-derived tropospheric temperature trends to the diurnal cycle adjustment. *Journal of Climate*, 29(10), 3629–3646. <https://doi.org/10.1175/JCLI-D-15-0744.1>
- Menzel, W., Frey, R., Borbas, E., Baum, B. A., Cureton, G., & Bearson, N. (2016). Reprocessing of HIRS satellite measurements from 1980 to 2015: Development toward a consistent decadal cloud record. *Journal of Applied Meteorology and Climatology*, 55(11), 2397–2410. <https://doi.org/10.1175/JAMC-D-16-0129.1>
- Muller, R., Kunz, A., Hurst, D., Rold, C., Kramer, M., & Riese, M. (2016). The need for accurate long-term measurements of water vapor in the upper troposphere and lower stratosphere with global coverage. *Earth's Future*, 4(2), 25–32. <https://doi.org/10.1002/2015EF000321>
- Nalli, N., Jung, J., Stegmann, P., Johnson, B., & Zhou, L. (2022). Temperature-dependent optical constants of water in the thermal infrared derived from data archaeology. *Opt. Cont.*, 1(4), 738–746. <https://doi.org/10.1364/OPTCON.450833>

- Newman, S., Smith, J., Glew, M., Rogers, S., & Taylor, J. (2005). Temperature and salinity dependence of sea surface emissivity in the thermal infrared. *Quarterly Journal of the Royal Meteorological Society*, 131(610), 2539–2557. <https://doi.org/10.1256/qj.04.150>
- NOAA Physical Sciences Laboratory. (2011). Extended multivariate ENSO index (MEI.ext). (Tech. Rep.). Retrieved from <https://psl.noaa.gov/ens/mei.ext:NOAA-ESRL>
- Palchetti, L., Brindley, H., Bantges, R., Buehler, S. A., Camy-Peyret, C., Carli, B., et al. (2020). FORUM: Unique far-infrared satellite observations to better understand how Earth radiates energy to space. *Bulletin of the American Meteorological Society*, 101(12), E2030–E2046. <https://doi.org/10.1175/BAMS-D-19-0322.1>
- Peters, W., Jacobson, A., Sweeney, C., Tans, P., Conway, T. J., Masarie, K., et al. (2007). An atmospheric perspective on North American carbon dioxide exchange: CarbonTracker. *Proceedings of the National Academy of Sciences*, 104(48), 18925–18930. <https://doi.org/10.1073/pnas.0708986104>
- Prakash, S., & Norouzi, H. (2020). Land surface temperature variability across India: A remote sensing satellite perspective. *Theoretical and Applied Climatology*, 139(1–2), 773–784. <https://doi.org/10.1007/s00704-019-03010-8>
- Raghuraman, S., Paynter, D. V. R., Menzel, R. H. X., & Huang, X. (2023). Greenhouse gas forcing and climate feedback signatures identified in hyperspectral infrared satellite observations. *Geophysical Research Letters*, 50(24). <https://doi.org/10.1029/2023GL103947>
- Rodgers, C. (2000). *Inverse methods for atmospheric sounding* (p. 256). World Scientific.
- Roemer, F., Buehler, S., Brath, M., Kluft, L., & John, V. (2023). Direct observation of Earth's spectral long-wave feedback parameter. *Nature Geoscience*, 16(5), 416–421. <https://doi.org/10.1038/s41561-023-01175-6>
- Santer, B., Wigley, M., Boyle, J., Gaffen, D., Hnilo, J., Nychka, D., et al. (2000). Statistical significance of trends and trend differences in layer-average atmospheric temperature time series. *Journal of Geophysical Research*, 105(D6), 7337–7356. <https://doi.org/10.1029/1999JD901105>
- Santer, B. D., Taylor, K. E., Wigley, T. M. L., Johns, T. C., Jones, P. D., Karoly, D. J., et al. (1996). A search for human influences on the thermal structure of the atmosphere. *Nature*, 382(6586), 39–46. <https://doi.org/10.1038/382039a0>
- Schneider, P., an O'Gorman, T., & Levine, X. (2010). Water vapor and the dynamics of changes. *Reviews of Geophysics*, 48(3). <https://doi.org/10.1029/2009RG000302>
- Shao, X., Ho, S.-P., Jung, X., Zhou, Z., Chen, Y., Liu, T.-C., et al. (2023). Characterizing the tropospheric water vapor spatial variation and trend using 2007–2018 COSMIC radio occultation and ECMWF reanalysis data. *Atmospheric Chemistry and Physics*, 23, 14187–14218. <https://doi.org/10.5194/acp-23-14187-2023>
- Sherwood, S., Ingram, W., Tshushima, Y., Satoh, M., Roberts, M., Vidale, P., & O'Gorman, P. (2010). Relative humidity changes in a warmer climate. *Journal of Geophysical Research*, 115(D9). <https://doi.org/10.1029/2009JD012585>
- Shi, L., & Bates, J. (2011). Three decades of intersatellite-calibrated high-resolution infrared radiation sounder upper tropospheric water vapor. *Journal of Geophysical Research*, 116(D4), D04108. <https://doi.org/10.1029/2010JD014847>
- Smith, N., & Barnett, C. (2019). Uncertainty characterization and propagation in the community long-term infrared microwave combined atmospheric product system (CLIMCAPS). *Remote Sensing*, 11(10), 1227–1251. <https://doi.org/10.3390/rs11101227>
- Smith, N., & Barnett, C. (2020). CLIMCAPS observing capability for temperature, moisture, and trace gases from AIRS/AMSU and CrIS/ATMS. *Advanced Manufacturing Technology*, 13(8), 4437–4459. <https://doi.org/10.5194/amt-13-4437-2020>
- Smith, N., & Barnett, C. (2023). Practical implications of CLIMCAPS cloud clearing and derived quality metrics. *Earth and Space Science*, 10(6), e2023EA002913. <https://doi.org/10.1029/2023EA002913>
- Soden, B., & Held, I. (2006). An assessment of climate feedbacks in coupled ocean-atmosphere models. *Journal of Climate*, 19(14), 3354–3360. <https://doi.org/10.1175/jcli3799.1>
- Soden, B., Jackson, D. L., Ramaswamy, V., Schwarzkopf, M. D., & Huang, X. (2005). The radiative signature of upper tropospheric moistening. *Science*, 310(5749), 841–844. <https://doi.org/10.1126/science.1115602>
- Strow, L., & DeSouza-Machado, S. (2020). Establishment of AIRS climate-level radiometric stability using radiance anomaly retrievals of minor gases and sea surface temperature. *Atmospheric Measurement Techniques*, 13(9), 4619–4644. <https://doi.org/10.5194/amt-13-4619-2020>
- Strow, L., Hannon, S., DeSouza-Machado, S., Tobin, D., & Motteler, H. (2003). An overview of the AIRS radiative transfer model. *IEEE Transactions on Geosciences and Remote Sensing*, 41(2), 303–313. <https://doi.org/10.1109/tgrs.2002.808244>
- Strow, L., Hannon, S., Weiler, M., Overoye, K., Gaiser, S., & Ammann, H. (2003). Pre-launch spectral calibration of the Atmospheric InfraRed Sounder (AIRS). *IEEE Transactions on Geosciences and Remote Sensing*, 41(2), 274–286. <https://doi.org/10.1109/tgrs.2002.808245>
- Strow, L., Hepplewhite, C., Motteler, H., Buczkowski, S., & DeSouza-Machado, S. (2021). A climate hyperspectral infrared radiance product (CHIRP) combining the AIRS and CrIS satellite sounding record. *Remote Sensing*, 13(3), 418. <https://doi.org/10.3390/rs13030418>
- Susskind, J., Barnett, C., & Blaisdell, J. (2003). Retrieval of atmospheric and surface parameters from AIRS/AMSU/HSB data under cloudy conditions. *IEEE Transactions on Geosciences and Remote Sensing*, 41(2), 390–409. <https://doi.org/10.1109/tgrs.2002.808236>
- Susskind, J., Blaisdell, J., & Iredell, L. (2014). Improved methodology for surface and atmospheric soundings, error estimates, and quality control procedures: The atmospheric infrared sounder science team version-6 retrieval algorithm. *Journal of Applied Remote Sensing*, 8(1), 084994. <https://doi.org/10.1117/1.JRS.8.084994>
- Susskind, J., & Kouvaris, L. (2006). Contribution of the AIRS shortwave sounding channels to retrieval accuracy. In *Algorithms and technologies for multispectral, hyperspectral, and ultraspectral imagery XII* (Vol. 6233). <https://doi.org/10.1117/12.665061.62331A>
- Teixeira, J., Wilson, R., & Thrastarson, H. (2024). Direct observational evidence from space of the effect of CO₂ increase on longwave spectral radiances: The unique role of high-spectral-resolution measurements. *Atmospheric Chemistry and Physics*, 24(10), 6375–6383. <https://doi.org/10.5194/acp-24-6375-2024>
- Thorne, P., Lanzante, J., Peterson, T., Seidel, D. J., & Shine, K. (2011). Tropospheric temperature trends: History of an ongoing controversy. *Wiley Interdisciplinary Reviews: Climate Change*, 2(1), 66–88. <https://doi.org/10.1002/wcc.80>
- Tian, B. E. M., Roman, J., Thrastarson, H., Fetzer, R., & ad Monarrexz, E. (2020). *Airs version 7 level 3 product user guide*. (Tech. Rep.). Jet Propulsion Laboratory, California Institute of Technology. Retrieved from https://docsserver.gesdisc.eosdis.nasa.gov/public/project/AIRS/V7_L3_User_Guide.pdf
- van der Ent, R. J., & Tuinenburg, O. A. (2017). The residence time of water in the atmosphere revisited. *Hydrology and Earth System Sciences*, 21(2), 779–790. <https://doi.org/10.5194/hess-21-779-2017>
- Warner, J., Wei, Z., Strow, L., Dickerson, R. R., & Nowak, J. (2016). The global tropospheric ammonia distribution as seen in the 13-year AIRS measurement record. *Advanced Manufacturing Technology*, 16(8), 5467–5479. <https://doi.org/10.5194/acp-16-5467-2016>
- Whitburn, S., Clarisse, L., Bouillon, M., Safieddine, S., George, M., Dewitte, S., et al. (2021). Trends in spectrally resolved outgoing longwave radiation from 10 years of satellite measurements. *NPJ climate and atmospheric science*, 4(1), 48. <https://doi.org/10.1038/s41612-021-00205-7>

- Wu, W., Liu, X., Lei, X., and Xiong, L., Yang, Q., Yue, Q., et al. (2023). Single field-of-view sounder atmospheric product retrieval algorithm: Establishing radiometric consistency for hyper-spectral sounder retrievals. *Advanced Manufacturing Technology*, 16(20), 4807–4832. <https://doi.org/10.5194/amt-16-4807-2023>
- Zhou, D., Larar, A., Liu, X., Smith, W., Strow, L., Yang, P., et al. (2011). Global land surface emissivity retrieved from satellite ultraspectral IR measurements. *IEEE Transactions on Geoscience and Remote Sensing*, 49(4), 1277–1290. <https://doi.org/10.1109/tgrs.2010.2051036>
- Zou, M., Xiong, X., Wu, Z., Li, S., Zhang, Y., & Chen, L. (2019). Increase of atmospheric methane observed from space-borne and ground-based measurement. *Remote Sensing*, 11(8), 16. <https://doi.org/10.3390/rs11080964>